Material Matters™

ALDRICH®
Materials Science

10 years
2006 — 2015

Alternative Energy Generation and Storage

Materials for a Greener Tomorrow

THIOLATED GOLD NANOCLUSTERS:
A NEW CLASS OF PHOTOSENSITIZERS

TITANIA NANOTUBES
FOR SYNTHESIS AND APPLICATIONS

MOLYBDENUM DISULFIDE
UNDERSTANDING HYDROGEN EVOLUTION CATALYSIS

PERFLUOROSULFONIC ACID MEMBRANES
FOR FUEL CELL AND ELECTROLYSER APPLICATIONS

OLIVINE-TYPE CATHODE MATERIALS
FOR LITHIUM-ION BATTERIES

SIGMA-ALDRICH®

Introduction

Welcome to the third issue of *Material Matters*™ for 2015 focusing on alternative energy generation and storage. Energy is vital for economic and social growth and, traditionally, these have been empowered mostly by the conventional carbon-based fossil fuels. However, it has become apparent that conventional resources are not limitless and alternative renewable energy based on solar, wind, and hydrogen are a must to meet future energy demands.

The prospect of alternative energy being a viable contributor to the global energy needs vastly depends on two factors. First, the efficiency of energy generation must increase to render it cost-effective. Second, is the development of high energy density storage systems, as most of the renewable energy sources are intermittent in nature. Solar energy represents the largest segment of the available non-carbon-based energy source, and recently there has been a tremendous effort in harvesting using photovoltaic and photocatalytic techniques. Due to their high energy density storage capacities, lithium-ion batteries have attracted significant attention in recent years. Some important classes of materials with applications in solar energy harvesting and lithium-ion batteries are discussed in this issue.

In our first article, Prof. Prashant V. Kamat (University of Notre Dame, USA) discusses gold nanoclusters. It has been emphasized that metallic nanoclusters exhibit a long-lived excited state and their electronic and optical properties can be tuned by varying the coordinating ligand and/or by adjusting the number of atoms in the cluster core. The optical and photovoltaic properties of various gold nanoclusters are reviewed.

In the second article, Prof. Eugen Panaitescu and Prof. Laitka Menon (Northeastern University, USA) elaborate on the synthesis and applications of titania nanotubes. Application of titania nanotubes in photocatalysis and photovoltaics has been discussed in detail.

Prof. Linyou Cao (North Carolina State University, USA), in the third article, reviews the compositional and structural dependence of the catalytic properties of molybdenum sulfide. A perspective on the rational design behind high-performance cost-effective catalysts for hydrogen evolution is presented.

In the fourth article, Prof. Deborah Jones (University of Montpellier, France) reviews the compositional and structural differences of various perfluorosulfonic acid membranes used in proton-exchange membrane fuel cells and electrolysers. In particular, the importance of the short side chain in determining the stability and durability of membranes is highlighted.

Finally, in fifth article Prof. Izumi Taniguchi (Tokyo Institute of Technology, Japan) reviews the electrochemical properties of olivine-type cathode materials for lithium-ion batteries. $LiMPO_4/C$ nanocomposites synthesized using a combination of spray pyrolysis, ball milling, and heat treatment show excellent electrochemical properties and are promising cathode materials.

Each article in this publication is accompanied by a list of relevant materials available from Aldrich® Materials Science. For additional product information, visit us at aldrich.com/matsci. Send your comments or suggestions for *Material Matters*™ or your product suggestions to matsci@sial.com. We look forward to hearing from you.

Niraj Singh, Ph.D.
Aldrich Materials Science

About Our Cover

Advancements in alternative energy generation and storage are critical for meeting future energy demands as well as for reducing our carbon footprint. These could be achieved through materials innovation. The background of the cover art represents two-dimensional materials, such as molybdenum disulfide and grapheme, which find a variety of applications in the aforementioned technologies. The presence of solar panels and energy storage devices on the cover art emphasizes the importance of innovations in both technologies, whereas the presence of flowers highlights the fact that a combination of both alternative energy generation and storage technologies would lead to a cleaner environment. Aldrich® Materials Science is proud to help enable these alternative energy and storage technologies with a large variety of innovative materials.

Table of Contents

Articles

Featured Products

Your Materials Matter

Bryce P. Nelson, Ph.D.
Aldrich Materials Science Initiative Lead

We welcome fresh product ideas. Do you have a material or compound you wish to see featured in the Aldrich® Materials Science line? If it is needed to accelerate your research, it matters. Send your suggestion to **matsci@sial.com** *for consideration.*

Dr. Benoit Simard of the National Research Council (Canada) recommended the addition of Boron Nitride Nanotubes (BNNTs, **Aldrich Prod. No.** 802824) to our catalog. BNNTs are wide band gap analogs of carbon nanotubes with high chemical, thermal, and mechanical stability. They find applications in transparent materials, bulk composites and assemblies, spintronics, gas adsorption, and others.[1-5] BNNTs are also being actively investigated for diagnostics and drug delivery applications.[6]

References

(1)	Kim, K. S.; Kingston, C. T.; Hrdina, A.; Jakubinek, M. B.; Guan, J.; Plunkett, M.; Simard, B. *ACS Nano* **2014**, *8*, 6211.
(2)	Fathalizadeh, A.; Pham, T.; Mickelson, W.; Zettl, A. *Nano Lett.* **2014**, *14*, 4881.
(3)	Dhungana, K. B.; Pati, R. *Sensors* **2014**, *14*(9), 17655.
(4)	Golberg, D.; Bando, Y.; Tang, C.; Zhi, C. *Adv. Mater.* **2007**, *19*, 2413.
(5)	Kim, K. S.; Jakubinek, M. B.; Martinez-Rubi, Y.; Ashrafi, B.; Guan, J.; O'Neill, K.; Plunkett, M.; Hrdina, A.; Lin, S.; Denommee, S.; Kingston, C.; Simard, B. *RSC Advances* **2015**, *5*, 41186.
(6)	Ciofani, G.; Danti, S.; Genchi, G. G.; Mazzolai, B.; Mattoli, V. *Small* **2013**, *9*, 1672.

Boron nitride nanotubes

BN   FW 24.82
BNNT nanotubes

BNNT: >50%
Diameter: ~5 nm
Surface area: >100 m^2/g

802824-250MG	250 mg
802824-1G	1 g

MAKE YOUR OWN LITHIUM-ION BATTERIES

Applications of lithium-ion batteries (LIBs) extend from modern electronics to automobiles. Order ready-to-use electrolyte solutions and electrode sheets in battery grade to fabricate your LIB.
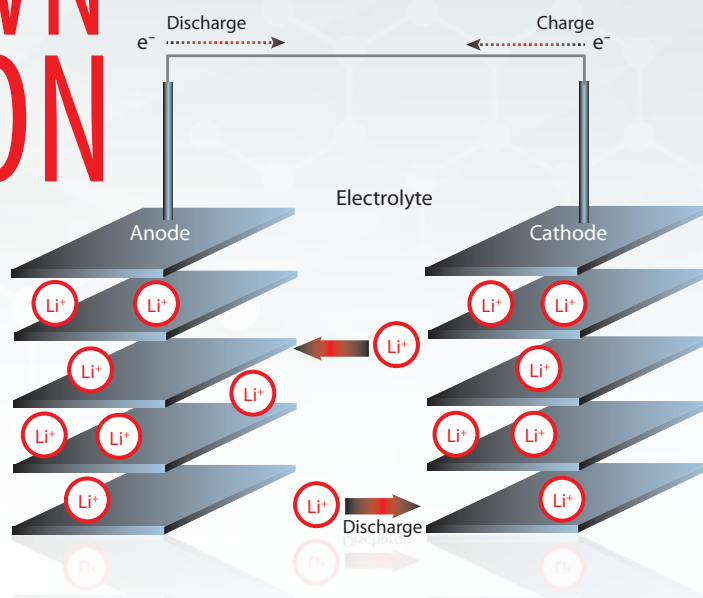
Electrolyte Solutions

Lithium Hexafluorophosphate Solutions, H_2O <15 ppm; HF <50 ppm; APHA <50

Name	Specifications	Prod. No.
1.0 M $LiPF_6$ in EC/DMC=50/50 (v/v)	in ethylene carbonate and dimethyl carbonate, battery grade	746711
1.0 M $LiPF_6$ in EC/EMC=50/50 (v/v)	in ethylene carbonate and ethyl methyl carbonate, battery grade	746738
1.0 M $LiPF_6$ in EC/DEC=50/50 (v/v)	in ethylene carbonate and diethyl carbonate, battery grade	746746
1.0 M $LiPF_6$ in DMC	in dimethyl carbonate, battery grade	746754
1.0 M $LiPF_6$ in EMC	in ethyl methyl carbonate, battery grade	746762
1.0 M $LiPF_6$ in DEC	in diethyl carbonate, battery grade	746770
1.0 M $LiPF_6$ in PC	in propylene carbonate, battery grade	746789

Electrode Sheets

Sheet size 5 × 10 in./80% active material on aluminum electrode substrate

Name	Specifications	Composition	Prod. No.
Lithium nickel manganese cobalt oxide	aluminum substrate, size 5 in. × 10 in., loading >80%, thickness 25–50 μm	$LiNi_{0.33}Mn_{0.33}Co_{0.33}O_2$	765163
Lithium nickel cobalt aluminum oxide	aluminum substrate, size 5 in. × 10 in., loading >80%, thickness 12–25 μm	$LiNi_{0.8}Co_{0.15}Al_{0.05}O_2$	765171
Lithium manganese nickel oxide	aluminum substrate, size 5 in. × 10 in., loading >80%, thickness 25–50 μm	$Li_2Mn_3NiO_8$	765198
Lithium manganese oxide	aluminum substrate, size 5 in. × 10 in., loading >80%, thickness 25–40 μm	$LiMn_2O_4$	765201
Lithium titanate spinel	aluminum substrate, size 5 in. × 10 in., loading >80%, thickness 25–50 μm	$Li_4Ti_5O_{12}$	765155

For a complete list of LIB materials, including electrode powders, electrolytes, solvents and additives, visit
aldrich.com/lib

THIOLATED GOLD NANOCLUSTERS:
A NEW CLASS OF PHOTOSENSITIZERS

Kevin Stamplecoskie, Yong-Siou Chen, Prashant V. Kamat*
Radiation Laboratory and Department of Chemistry and Biochemistry
University of Notre Dame, Notre Dame, Indiana, USA
*Email: pkamat@nd.edu

Introduction

The past several decades have seen major advancements in the synthesis of metal nanomaterials. Most recently, controlled synthesis has become versatile enough to regulate the exact number of atoms and ligands of very small metal nanoparticles, referred to as "clusters". Unlike metal nanoparticles or even bulk metal, these clusters display interesting optical properties such as intense photoluminescence. The luminescence arises from discrete electronic energy level transitions that are available only in such extremely small particles. For this reason, clusters are considered to be molecule-like, behaving very different from other forms of metals. Clusters serve as a unique bridge between the single-atom limit and well-understood bulk materials. Due to their small size, the electronic and optical properties of clusters are drastically affected by the exact number of metal atoms that comprise their core and by the choice of coordinating ligand. The tunability with size/composition opens many new opportunities for using these clusters in fluorescence, such as biological imaging. Their long-lived excited states also make them an attractive new class of light absorbers for light-harvesting and energy applications.

Photovoltaic Properties of Gold Clusters

One commonly studied class of clusters is thiolate protected gold clusters, with the molecular formula Au_xSR_y. Many variations of these clusters have been made by varying the atom counts for the metal (x) as well as through the use of different types of coordinating thiols (y). For example, the most commonly synthesized/studied cluster has the formula $Au_{25}SR_{18}$ (25 gold atoms and 18 thiol ligands). The structure of $Au_{25}SR_{18}$, as well as other cluster sizes such as $Au_{38}SR_{24}$ and $Au_{144}SR_{60}$, have been determined by single crystal X-ray diffraction (XRD), illustrated in **Figure 1**. $Au_{144}SR_{60}$ displays molecule-like electronic properties, with discrete electronic states. Above this size, however, the number of atoms in the core is so large that their discrete electronic states are not distinguishable, and they behave as a metal with a full band structure. The optical absorption of particles larger than $Au_{144}SR_{60}$ is dominated by plasmon absorptions arising from collective oscillations of loosely bound electrons.
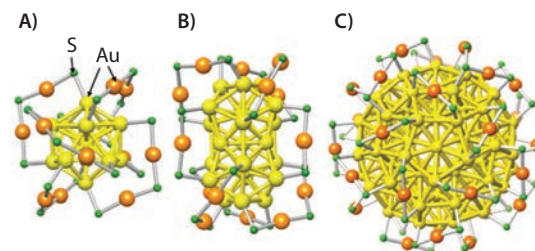
Figure 1. Crystal structure of **A)** $Au_{25}SR_{18}$, **B)** $Au_{38}SR_{24}$, and **C)** $Au_{144}SR_{60}$ as determined by XRD. The ligands have been omitted for clarity, only showing the S atoms (green). Reproduced with permission from Reference 1. Copyright American Chemical Society.

Due to the small size of atomically precise clusters, the photophysical properties are strongly dependent on the exact number of metal atoms. In a recent study we have shown that the ability to absorb sunlight and the ability to convert sunlight to energy in photovoltaics is drastically influenced by the number of atoms.[3] **Figure 2** shows the absorption spectra of a series of glutathione-protected clusters containing different numbers of metal atoms (Au_{11}, Au_{15}, Au_{18}, and Au_{25}). In addition to the light absorption properties, the excited state behavior is also important in determining the light-harvesting potential of a light absorbing material. We are only beginning to understand the optical properties and excited state behavior of these clusters. A better understanding of their behavior promises new opportunities for discovery and optimization of materials for light-harvesting applications.
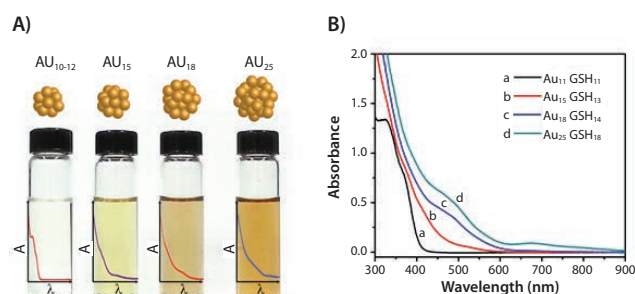
Figure 2. A) Different size cluster suspensions and **B)** corresponding absorption spectra. Reproduced with permission from Reference 3.

Thiolated gold clusters do not exhibit plasmon resonance like larger size metal nanoparticles. They absorb visible light as indicated by the absorption spectra in **Figure 2**. With an increasing number of gold atoms, the absorption extends into the visible spectra. These clusters are highly photoactive and exhibit a long excited state lifetime (~780 ns).[2] In smaller gold clusters, the ligand-to-metal charge complex dominates the excited state. In larger clusters (e.g., $Au_{25}GSH_{18}$) the core transitions contribute to the excited state decay and, thus, decrease the excited state lifetime. More detailed photophysical characterization of these gold clusters can be found elsewhere.[3]

For questions, product data, or new product suggestions, contact us at **matsci@sial.com**.

71

The rich photochemistry of glutathione-capped gold clusters has enabled a new class of photosensitizers. Light harvesting in these gold clusters is made possible through the transfer of electrons to molecular species like methyl viologen. We have used transient absorption spectroscopy to establish the mechanistic and kinetic aspects of the photoinduced electron transfer processes in suspensions of these gold clusters.[2–3]

An important application of these gold clusters is in the area of light-energy conversion. We have explored the photosensitizing ability of gold clusters by attaching them to mesoscopic titanium dioxide (TiO$_2$) films. Au$_x$-SH modified TiO$_2$ mesoscopic films respond well to visible light excitation when employed as the photoanode in liquid-junction solar cells. Photocurrent action spectra of the metal cluster sensitized solar cell (MCSC) and cadmium sulfide (CdS)-based liquid-junction solar cells are compared in **Figure 3**. The photocurrent response matches well with the absorption of Au$_x$-SH clusters. The maximum incident photon-to-photocurrent efficiency (IPCE) of 70% observed at 400–425 nm shows the gold clusters can harvest incident photons and efficiently convert them to electrical energy. These MCSCs exhibit maximum power conversion efficiency in the range of 2.03–2.36%, which is comparable to CdS quantum dot solar cells.
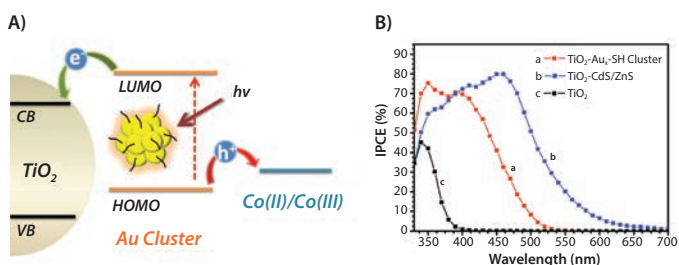
Figure 3. A) An illustration of the working principal of MCSCs. B) IPCE spectra (external quantum efficiency) of a photoelectrochemical cell using photoanodes composed of (a) TiO$_2$-Au$_x$-SH Cluster, (b) TiO2-CdS/ZnS, and (c) TiO$_2$. Reproduced with permission from Reference 4. Copyright American Chemical Society.

The gold cluster sensitized solar cells exhibit relatively high open circuit voltage (0.85–0.90 V) as compared to other sensitizing dyes. We have made use of gold nanoclusters to further boost the photovoltage of dye-sensitized solar cells employing a squaraine dye (**Aldrich Prod. No. 757233**) and ruthenium polypyridyl complex as photosensitizer.[5] An increase of ~100 mV is seen when gold clusters are co-anchored on TiO$_2$ (**Aldrich Prod. Nos. 799289**, **204757**, **232033**, and **248576**) with other sensitizing dyes. These beneficial effects are attributed to the shift in Fermi level to more negative potentials as a result of electron accumulation in metal cluster co-sensitized solar cells.

Another interesting property of the gold cluster is its redox property. Cyclic voltammetry experiments have shown a large window for reversible reduction [E^0= -0.63 V vs. RHE (reversible hydrogen electrode)] and oxidation (E^0= 0.97 V and 1.51 V vs. RHE) processes. This property has further been explored to generate hydrogen in both

photoelectrochemical cells and photocatalytic slurry systems (**Figure 4**). By anchoring the gold clusters on TiO$_2$ particles, it is possible to inject electrons into TiO$_2$ under visible light irradiation. These injected electrons were transferred to an active platinum catalyst site to reduced H$^+$ ions into hydrogen. More details on the mechanistic aspects of solar fuel generation can be found elsewhere.[6]
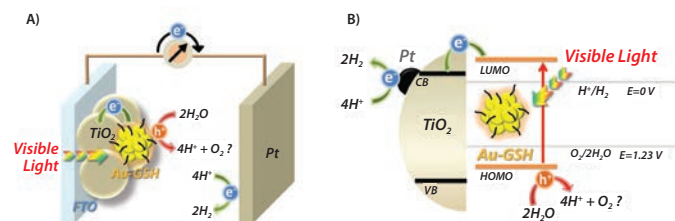
Figure 4. Schematic of the working principle of (**A**) Au$_x$-GSH sensitized TiO$_2$ film as a photoanode of a photoelectrochemical cell (PEC) and (**B**) Au$_x$-GSH sensitized Pt/TiO$_2$ NPs photocatalytic system for water-splitting reaction under visible light illumination. Reproduced with permission from Reference 6. Copyright American Chemical Society.

Summary

We have presented some interesting aspects of gold atom nanoclusters. The excellent photosensitizing ability of gold clusters renders them promising for light energy harvesting applications. Additionally, the high photoactivity, stability in aqueous medium, and biocompatibility make these clusters suitable as biotags or biomarkers.[7] Since these photosensitizers are relatively new, efforts are still needed to explore them in energy generation and biological applications. As the scientific community explores to new design metal clusters with tailored ligands, one can expect additional applications of these metal clusters.

Acknowledgment

References
(1) Kurashige, W.; Niihori, Y.; Sharma, S.; Negishi, Y. *J. Phys. Chem. Lett.* **2014**, *5*, 4134–4142.
(2) Stamplecoskie, K. G.; Chen, Y. S.; Kamat, P. V. *J. Phys. Chem. C* **2014**, *118*, 1370–1376.
(3) Stamplecoskie, K. G.; Kamat, P. V. **2014**, *136*, 11093–11099.
(4) Chen, Y. S.; Choi, H.; Kamat, P. V. *J. Am. Chem. Soc.* **2013**, *135*, 8822–5.
(5) Choi, H.; Chen, Y.-S.; Stamplecoskie, K. G.; Kamat, P. V. *J. Phys. Chem. Lett.* **2015**, *6*, 217–223.
(6) Chen, Y. S.; Kamat, P. *J. Am. Chem. Soc.* **2014**, *136*, 6075–6082.
(7) Retnakumari, A.; Setua, S.; Menon, D.; Ravindran, P.; Muhammed, H.; Pradeep, T.; Nair, S.; Koyakutty, M. *Nanotechnology* **2010**, *21*, 055103.

Core-type Quantum Dots

For a complete list of core-type quantum dots, visit aldrich.com/quantumdots.

PbS

Product Name	Description	Fluorescence Emission (λ_{em} in nm)	Prod. No.
PbS core-type quantum dots	10 mg/mL in toluene; oleic acid coated	1000	747017-10ML
	10 mg/mL in toluene; oleic acid coated	1200	747025-10ML
	10 mg/mL in toluene; oleic acid coated	1400	747076-10ML
	10 mg/mL in toluene; oleic acid coated	1600	747084-10ML

CdSe

Product Name	Description	Fluorescence Emission (λ_{em} in nm)	Prod. No.
Lumidot™ CdSe	5 mg/mL in toluene; 2.1 - 2.3 nm	475-485	662356-10ML
	5 mg/mL in toluene; 2.4 - 2.6 nm	515-525	662437-10ML
	5 mg/mL in toluene; 3.0 - 3.5 nm	555-565	662445-10ML
	5 mg/mL in toluene; 4.0 - 4.3 nm	585-595	662607-10ML
	5 mg/mL in toluene; 4.7 - 5.2 nm	605-615	662488-10ML
	5 mg/mL in toluene; 6.2 - 7.7 nm	635-645	662461-10ML
Lumidot™ CdSe-6, quantum dot nanoparticles kit	5 mg/mL in toluene	480-640	662550-1KT

CdTe

Product Name	Description	Fluorescence Emission (λ_{em} in nm)	Prod. No.
CdTe core-type quantum dots	COOH functionalized; powder	510	777986-10MG 777986-25MG
	COOH functionalized; powder	520	777935-10MG 777935-25MG
	COOH functionalized; powder	570	777943-10MG 777943-25MG
	COOH functionalized; powder	610	777951-10MG 777951-25MG
	COOH functionalized; powder	710	777978-10MG 777978-25MG
	COOH functionalized; powder	770	777994-10MG 777994-25MG

Core-shell Type Quantum Dots

For a complete list of core-shell quantum dots, visit aldrich.com/quantumdots.

CdSe/ZnS

Product Name	Description	Fluorescence Emission (λ_{em} in nm)	Prod. No.
CdSe/ZnS core-shell type quantum dots	stabilized with octadecylamine ligands; solid	520	748021-10MG 748021-25MG
	stabilized with octadecylamine ligands; solid	540	748056-10MG 748056-25MG
	stabilized with octadecylamine ligands; solid	560	748080-10MG 748080-25MG
	stabilized with octadecylamine ligands; solid	580	748129-10MG 748129-25MG
	stabilized with octadecylamine ligands; solid	600	748099-10MG 748099-25MG
	stabilized with octadecylamine ligands; solid	620	790192-10MG 790192-25MG
	stabilized with octadecylamine ligands; solid	630	790206-10MG 790206-25MG

InP/ZnS

Product Name	Description	Fluorescence Emission (λ_{em} in nm)	Prod. No.
InP/ZnS quantum dots	5 mg/mL in toluene; stabilized with oleylamine ligands	530	776750-5ML
	5 mg/mL in toluene; stabilized with oleylamine ligands	560	776793-5ML
	5 mg/mL in toluene; stabilized with oleylamine ligands	590	776769-5ML
	5 mg/mL in toluene; stabilized with oleylamine ligands	620	776777-5ML
	5 mg/mL in toluene; stabilized with oleylamine ligands	650	776785-5ML

Alloyed Quantum Dots

For a complete list of alloyed quantum dots, visit aldrich.com/quantumdots.

Product Name	Description	Fluorescence Emission (λ_{em} in nm)	Prod. No.
CdSeS/ZnS alloyed quantum dots	1 mg/mL in toluene, diameter 6 nm	450	753742-5ML 753742-25ML
	1 mg/mL in toluene, diameter 6 nm	490	753750-5ML 753750-25ML
	1 mg/mL in toluene, diameter 6 nm	525	753769-5ML 753769-25ML
	1 mg/mL in toluene, diameter 6 nm	540	753777-5ML 753777-25ML
	1 mg/mL in toluene, diameter 6 nm	575	753785-5ML 753785-25ML
	1 mg/mL in toluene, diameter 6 nm	630	753793-5ML 753793-25ML
	1 mg/mL in toluene, diameter 6 nm	665	753807-5ML 753807-25ML
	1 mg/mL in H_2O, diameter 6 nm, COOH functionalized	490	754226-1ML 754226-5ML
	1 mg/mL in H_2O, diameter 6 nm, COOH functionalized	525	753831-1ML 753831-5ML
	1 mg/mL in H_2O, diameter 6 nm, COOH functionalized	540	753866-1ML 753866-5ML
	1 mg/mL in H_2O, diameter 6 nm, COOH functionalized	575	753874-1ML 753874-5ML
	1 mg/mL in H_2O, diameter 6 nm, COOH functionalized	630	753882-1ML 753882-5ML
	1 mg/mL in H_2O, diameter 6 nm, COOH functionalized	665	753890-1ML 753890-5ML
CdSeS/ZnS alloyed quantum dots kit	5 x 1 mg/mL in H_2O, diameter 6 nm, COOH functionalized	490-665	753904-1KT
	5 x 1 mg/mL in toluene, diameter 6 mm	490-665	753823-1KT

Precursors for Organometallic Perovskites

For a complete list of perovskite precursors, visit aldrich.com/perovskites.

Product Name	Composition	Description	Prod. No.
Methanamine hydriodide	$CH_3NH_2 \cdot HI$	powder; 98%	793493-5G
Methanamine hydrobromide	$CH_3NH_2 \cdot HBr$	powder; 98%	793507-5G
Methylammonium triiodoplumbate(II) precursor solution	$[CH_3NH_3]^+[PbI_3]^-$	solution; 40 wt. % in DMF	793833-5ML
Lead(II) iodide solution	PbI_2	solution; 0.55 M in DMF	795550-10ML
Lead(II) iodide	PbI_2	beads; 99.999% trace metals basis	554359-5G
	PbI_2	solid; 99.999% trace metals basis	203602-50G
	PbI_2	powder; 99%	211168-50G
Lead(II) chloride	$PbCl_2$	beads; 99.999%	449865-5G
	$PbCl_2$	powder and chunks; 99.999% trace metals basis	203572-10G 203572-50G
	$PbCl_2$	powder; 98%	268690-5G 268690-250G 268690-1KG
Lead(II) bromide	$PbBr_2$	powder; 99.999% trace metals basis	398853-5G
	$PbBr_2$	powder; ≥98%	211141-100G 211141-500G

Titania Nanomaterials for Support

For a complete list of nanomaterials, visit aldrich.com/nanopowders.

Product Name	Description	Purity	Form	Prod. No.
Titanium	particle size <100 nm	98.5% trace metals basis	dispersion nanoparticles	513415-5G
Titanium dioxide	particle size 22 - 25 nm (BET) spec. surface area 65-75 m²/g (BET)	>95% (anatase (XRD))	nanoparticle paste	798495-25G
	particle size 18 - 20 nm (BET) spec. surface area 75-85 m²/g (BET)	-	nanoparticle paste	798509-25G
Titanium(IV) oxide	primary particle size 21 nm (TEM), surface area 35-65 m²/g (BET)	≥99.5% trace metals basis	nanopowder	718467-100G
Titanium(IV) oxide, anatase	particle size <25 nm, spec. surface area 45-55 m²/g	99.7% trace metals basis	nanopowder	637254-50G 637254-100G 637254-500G
Titanium(IV) oxide, mixture of rutile and anatase	particle size <100 nm (BET) particle size <50 nm (XRD)	99.5% trace metals basis	nanopowder	634662-25G 634662-100G
	particle size ~21 nm (primary particle size of starting nanopowder)	99.9% trace metals basis	nanoparticle paste	700355-25G
	particle size ~21 nm (primary particle size of starting nanopowder)	99.5% trace metals basis	dispersion nanoparticles	700347-25G 700347-100G
	particle size <100 nm (DLS)	99.9% trace metals basis	dispersion nanoparticles	700339-100G
Titanium(IV) oxide, rutile	particle size <100 nm, spec. surface area 50 m²/g	99.5% trace metals basis	nanopowder	637262-25G 637262-100G 637262-500G

BORON NITRIDE NANOTUBES

Boron nitride nanotubes (BNNTs) are structural analogs of carbon nanotubes and offer advantages such as:

- High stiffness
- Improved chemical stability
- Enhanced thermal conductivity
- High thermal stability
- Electric field tunable band gap

Applications of BNNTs extend from transparent materials, bulk composites and assemblies, to spintronics, gas adsorption, drug delivery, and diagnostics.

Aldrich® Materials Science offers induction plasma-processed BNNTs (**Aldrich Prod. No.** 802824) with:

- Diameter of ~5 nm
- Surface area >100 m^2/g
- BNNT >50%
- No metal catalyst
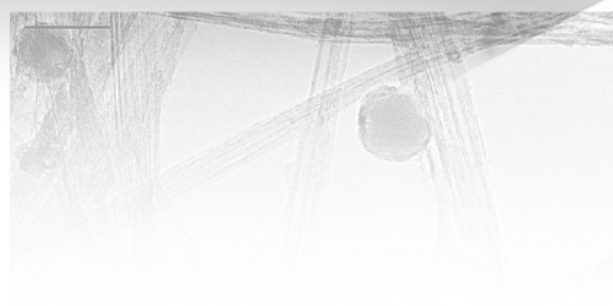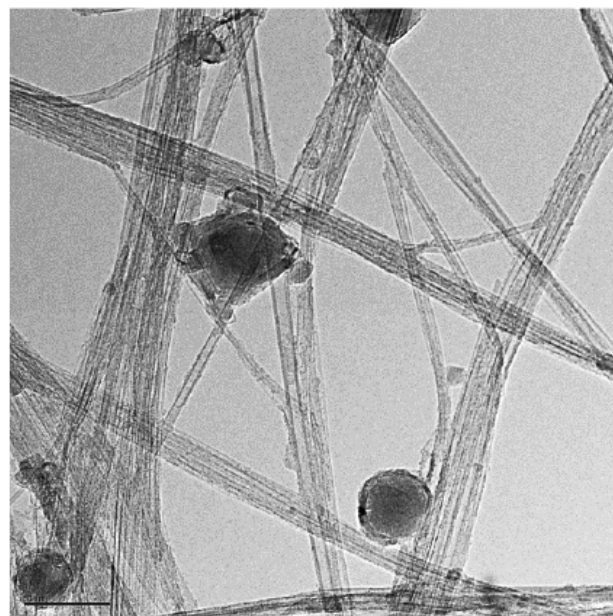
For the complete nanomaterials offering, visit
aldrich.com/nano

TITANIA NANOTUBES:
SYNTHESIS AND APPLICATIONS

Eugen Panaitescu[1] and Latika Menon[2]
Department of Physics
Northeastern University, Boston, MA 02115 USA
Email: [1]e.panaitescu@neu.edu, [2]l.menon@neu.edu

Introduction

Titania (titanium dioxide, TiO_2) (**Aldrich Prod. Nos.** 799289, 204757, 232033, 248576, and 677469) is a versatile earth-abundant ceramic with many desirable properties such as high melting point (>1,800 °C) and stability under adverse chemical conditions.[1] Electronically, it behaves as a wide band gap (3.2 eV) semiconductor and exhibits memristor properties.[2] Optically, TiO_2 has high opacity with a very high refractive index[3] (>2.4), and it exhibits strong absorbance in the UV range. It is an excellent catalyst because of its strong oxidative potential, especially when exposed to UV light. As a result of these properties, titania finds a wide range of applications in white/opaque pigments, coatings and sunscreens (protection from UV radiation), antifogging coatings,

ceramic filtration membranes, antimicrobial coatings, photocatalysis, and photovoltaics (e.g., dye-sensitized solar cells—DSCs). In the nanostructure form, titania exhibits additional features such as high porosity and surface area. For example, titania nanotubes (TiNT) (**Aldrich Prod. No.** 799289) possess high porosity (50–200 m²/g) and high active surface area (2–3 orders of magnitude higher than a flat surface). These features greatly enhance the efficiency of the aforementioned applications and make them suitable for new applications[4] like highly oleophobic filtration membranes for water-oil separation[5] and anodes for fast-charging lithium-ion batteries.[6] We have identified a wide array of potential applications for TiNT. A summary of some of these promising applications, either in as-is form or integrated with other (nano) materials and incorporated into complex structures or devices, is presented in **Table 1**.

Synthesis of Titania Nanotubes by Electrochemical Anodization

Historically, many different methods such as electrochemical deposition in nanoporous alumina templates,[7] sol-gel methods,[8] seeded growth,[9] electrospinning,[10] and hydrothermal methods have been employed for the synthesis of TiNT.[11] However, in general, these are complex, multi-step methods that are hard to scale up beyond lab scale and result in a low yield of nanotubes. Synthesis of TiNT by means of electrochemical anodization of titanium in fluoride-ion containing electrolytes was

Table 1. Summary of Potential Applications of Titania Nanotubes

		← Established Technologies ———— Novel Concepts Needing Industry Confirmation →		
TiNT-based Solar Cells • New paradigms • Solid-state DSC • Hybrid DSC • Traditional DSC	**Utilities (Residential/Commercial)** **Customer Need:** Low cost (grid parity) **Challenge:** Volatile PV market in US, decreasing cost of Si, long-term stability	**Portable/Flexible** *New Market (small hand-held devices)* **Customer Need:** Personalized solar power, light weight, flexible, low cost, all-time power for handheld devices		**Automobile/Building Integrated PV** *New Market* **Customer Need:** Low-cost, reliable, long lifetime solutions and integrability with steel, glass, etc.
TiNT for Lithium-ion Battery Anodes	**Batteries for Electrical Vehicles, Homes** **Customer Need:** Fast-charging, long lifetime			
TiNT Arrays-based Catalysts	**Hydrogen Generation** **Market Need:** High efficiency, low-cost generation (current technology in US is based on steam reformation)	**Catalysts for Fuel cells/Automobile Exhausts** **Customer Need:** Highly effective surface area, low cost, reliable, durable catalysts **Challenge:** Disruptive technology, hard-to-establish market point-of-entry		
As-synthesized TiNT Arrays • Pressed into pellets • Free-standing membranes • Single-tube dispersion	**Oil-Water Filtration/Separation** **Customer Need:** Low-cost and highly efficient solutions, robust materials for adverse chemical and temperature conditions	**Drug Delivery/Stents/Controlled Release Separation at the Micro and Nanoscale** **Customer Need:** Highly uniform, custom-synthesizable nanotubes offering controlled separation **Challenge:** May need FDA approval		
Minimally Processed TiNT Arrays • As-is TiNT arrays • Powders • Flakes • On-site anodization	**Food/Agriculture/Plastic Bags/Paint/Cosmetics/Jewelry** **Customer Need:** Highly effective surface area, custom-synthesizable TiNT arrays			**Implants (Dental/Bone/ Body)** **Challenge:** May need FDA approval

(Left axis top to bottom: ↑ Increasing Production Costs / ← Simpler Structures)

developed relatively recently.[12] This is a simple, cost effective, easily scalable method resulting in highly ordered arrays of vertically aligned nanotubes and has become the standard synthesis method for TiNTs. The mechanism for nanotube formation is very similar to that of nanopores in anodic aluminum oxide (AAO), a well-known and extensively reported material.[13] The synthesis of TiNT is initiated by the application of a DC bias voltage in the presence of the electrolyte containing both oxidizing and reducing agents to form an oxide layer on the surface of the metal anode (Al or Ti). This is followed by the field-enhanced dissolution of the oxide, which results in corrosion pits. When equilibrium between oxidation and dissolution is reached, the corrosion pits grow continuously into vertically aligned nanopores or nanotubes. Because nanotubes produced by anodization are amorphous, the samples must be annealed in air, oxygen, or a nitrogen atmosphere at 300–500 °C, with a slow heating and cooling rate (1–5 °C/min) to produce crystalline material. The resulting structure is anatase (polycrystalline) with a crystal size of approximately 25 nm.

A significant advantage of anodization over other fabrication methods is that it offers precise control over the shape, structure, and morphology of the produced nanotubes simply by controlling different synthesis parameters. For instance, anodization voltage can be used to control nanotube diameter, while the time of anodization can be modified to control the average length of the tubes. The viscosity, pH, and concentration of fluoride ions within the solution influence the oxide dissolution and rate of chemical reaction. These parameters have a direct effect on the tube formation rate, maximum achievable tube length, and smoothness of the tube walls. The water content controls the strength of the attachment between the nanotube arrays and the original Ti substrate. Some typical TiNT morphologies that may be obtained are listed below.

- Low Aspect Ratio TiNT Arrays (**Figure 1A**)
  Up to 6:1 aspect ratio (30–80 nm diameter, 100–500 nm length) TiNT arrays can be obtained by anodization for less than an hour at anodization voltages between 10 and 20 V DC in 0.1–0.4 M HF solutions. The tubes are quasi-ordered, form rapidly, and are uniformly distributed over the entire sample surface.

- High Aspect Ratio TiNT Arrays (**Figure 1B**)
  Up to 100:1 aspect ratio (50–150 nm diameter, 2–8 µm length) nanotube arrays can be obtained by anodization for 3–8 h at anodization voltages between 10 and 30 V DC in aqueous solutions containing fluoride salts (KF, NaF, NH_4F), buffered in order to lower the acidity (pH up to 4). Well-defined and well-ordered nanotubes arrays are produced. The key disadvantage of this method is the requirement of long anodization times.

- Ultra-high Aspect Ratio, Highly Ordered TiNT Arrays (**Figures 1C, D**)
  Over 1,000:1 aspect ratio (90–200 nm diameter, length up to mm range) nanotube arrays can be obtained by anodization at 30–60 V DC in non-aqueous solutions containing fluoride salts, using solvents such as formamide (**Sigma-Aldrich Prod. No.** F7503), DMSO (**Sigma-Aldrich Prod. Nos.** 276855 and 472301), ethylene glycol (**Sigma-Aldrich Prod. Nos.** 324558 and 102466) or glycerol (**Sigma-Aldrich Prod. Nos.** G5150 and G7757). Smooth, well-defined, and quasi-hexagonally ordered nanotubes are obtained. When the water content in the electrolyte is reduced to a minimum, the TiNT can detach from the Ti substrate, and free standing arrays of TiNT can be obtained (**Figure 1D**). Length of the nanotubes can be tailored by controlling the time of anodization and can range from approximately 15 µm for 2 h anodization to 30 µm after 6–8 h, and 50+ µm for over 24 h of anodization. In these cases, the maximum possible length of the nanotubes is typically limited by the thickness of the original Ti foil.
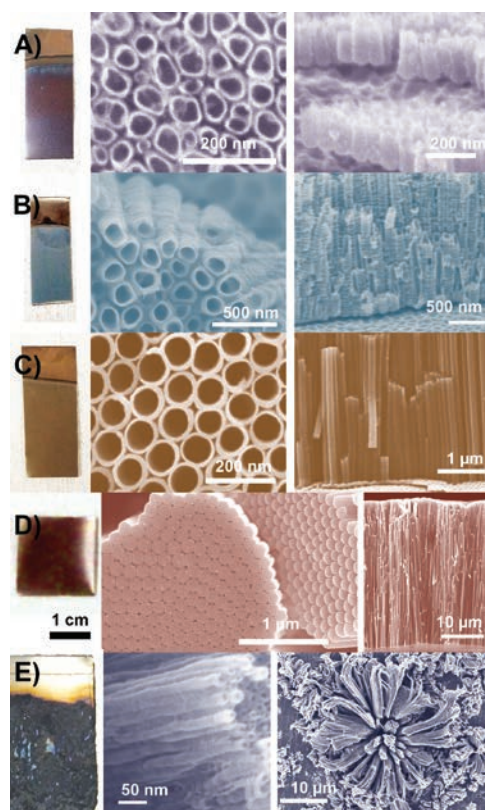
Figure 1. Digital pictures of the samples and frontal and side-view SEM images of titania nanotube samples fabricated in a variety of shapes and morphologies. **A**) Short nanotubes (<500 nm). **B**) Medium-length nanotubes (2–5 µm). **C**) Long and ultra-long nanotubes (30–700 µm) attached to the original support. **D**) Free-standing (bottom view shown here indicating that the tubes are closed, top view is similar with **C**). **E**) Ultra-long nanotube bundles (up to 60 µm) formed in corrosion pits scattered all over the sample.

Anodic TiNT arrays can be integrated with materials such as metals, metal-oxides, or polymers by various physical, chemical, electrochemical, or electrophoretic methods for optimized applications and devices.[4] For example, gold[14] (**Figures 2A, B**) (**Aldrich Prod. No.** 636347) or iron oxide (**Figures 2C, D**) nanoparticles (**Aldrich Prod. No.** 544884) can be easily attached to the nanotubes using simple deposition-precipitation methods.
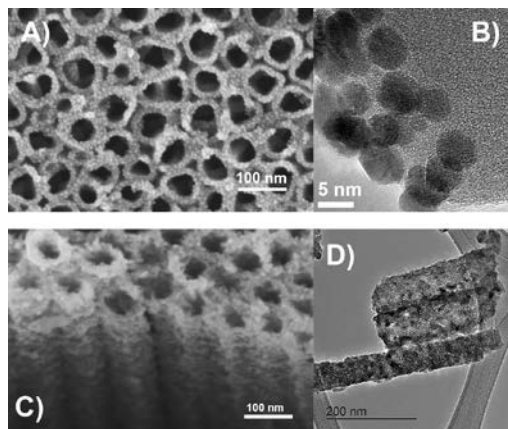
Figure 2. **A**) SEM and **B**) HRTEM images of TiNT arrays deposited with gold nanoparticles. **C**) SEM and **D**) TEM images of iron-oxide (hematite) decorated TiNT arrays.

Anodization in Chloride-ion Containing Solutions

Our recent work demonstrated the fluoride-ion electrochemistry-based nanotube formation mechanism can be replicated using chloride-ion containing solutions.[15] Besides eliminating the toxic fluorides from the synthesis process, the new method also results in significantly accelerated reaction rates,[16] reducing tube formation time from tens of minutes and hours to tens of seconds.[17] In this accelerated process, the corrosion pits evolve differently, and the titanium substrate does not have sufficient time to accommodate the increase in volume associated with the rapidly forming nanotubes. As a result, tightly bound nanotube bundles are expelled into the solution (**Figure 1E**), appearing as a white powder after washing and recovery from the solution. Bundles of nanotubes with an aspect ratio of over 1,000:1 (25–50 nm diameter, lengths up to 60 μm) can be obtained by anodization in aqueous (at DC voltages between 10 and 16 V) and non-aqueous solutions (at DC voltages between 30 and 60 V) containing chloride salts such as KCl, NaCl, or NH$_4$Cl. The bundles are tightly packed with cross-section areas varying from sub-microns (effectively containing a few tens of nanotubes) to a few square microns (with tens of thousands of nanotubes). Though ordering of the nanotubes is limited to a few tens of microns at most, and the coverage of the titanium foil with corrosion pits is not uniform, this method provides a much faster route for nanotube production. Gram quantities of ultra-high aspect ratio TiNT powders can be obtained after 60–100 min of anodization.

Applications: Photocatalysis

The photocatalytic properties of TiO$_2$ are based on its ability to generate electron-hole pairs under illumination, which then promote redox reactions such as electrolysis. The discovery of TiO$_2$-photocatalyzed water electrolysis in 1972[18] triggered enormous interest in the material for hydrogen production and for other photocatalytic applications. TiO$_2$ has been shown to be the most useful photocatalyst for numerous environmental applications due to its biological and chemical inertness, and resistance to photocorrosion and chemical corrosion. The three main photocatalysis applications—water splitting, organic compound decomposition, and inactivation of bacteria—are discussed in the following sections.

Hydrogen Generation by Water Photoelectrolysis

Photoelectrochemical generation of hydrogen by using TiNT has been studied extensively since the discovery of the new nanostructures 15 years ago. Park et al.[19] showed the nanotubular structure indeed enhances the photocatalytic activity of TiO$_2$ in water splitting by maximizing solar energy harvesting. Water splitting efficiency is significantly improved by optimizing structural and morphological parameters such as wall thickness, length, and crystalline structure (anatase) of the nanotubes. Band gap reduction by carbon doping or the addition of other metal oxides with narrower band gaps results in an increased hydrogen evolution rate. Our group demonstrated the adsorption of low quantities of sodium or potassium on the nanotube walls using sodium or potassium fluoride in the anodization solution used during the synthesis can result in increasing the overall efficiency of the photoelectrochemical process.[20]

Oxidation and Decomposition of Organic Compounds

The strong oxidation properties of titania under illumination can be employed in the decomposition of organic pollutants. The mechanism for degradation of organics is similar to that of water splitting. In aqueous solution electron-hole pairs are created in TiO$_2$ under exposure to a light source. These electron-hole pairs migrate to the surface and react with absorbed organic molecules, causing them to decompose. The photocatalytic activity exhibits more dependence on the specific surface area than the crystal phase of TiO$_2$. Efficient photoactivated demineralization of organic compounds by using membranes consisting of free-standing arrays of TiNT has also been demonstrated, opening the possibility for multifunctional, self-cleaning filtration membranes.[21]

Light-enhanced Antimicrobial Activity

TiO$_2$ has been used as a photocatalyst in antimicrobial applications as well. Under the irradiation of UV light, the generation of electrons at the conduction band and holes at the valence band in TiO$_2$ produce hydroxyl radicals (OH), superoxide radicals (O$_2$-), singlet oxygen (^{1}O$_2$), peroxide radicals (OOH), and hydrogen peroxide (H$_2$O$_2$). These reactive oxidation species result in physical damage to the cell membranes, leading to cell death. Recent work with TiNT powders performed by our group,[22] using *Escherichia coli (E. coli)* and *Staphylococcus aureus (S. aureus)* as the target microorganisms, revealed excellent antibacterial properties of the powders compared to commercial anatase nanoparticles (Degussa P25) (**Aldrich Prod. No. 718467**) after 24 h of UV exposure. Specifically, 97.53% of *E. coli* and 99.94% of *S. aureus* were destroyed after 24 h, while the commercial nanoparticle lost its antimicrobial properties after 1–6 h. Also, it was demonstrated the architecture, surface, and physicochemical properties of TiNT along with specific experimental conditions of the biological investigation, play a significant role in the disinfection activity.

Applications: Photovoltaics

The main application of nanostructured titania is in DSCs, one of the most promising among numerous third-generation photovoltaic technologies. DSCs provide acceptable solar energy conversion efficiency (>10%) by employing a much simpler structure, scalable fabrication route, and lower production costs compared to the silicon-based solar cells. Typical DSCs consist of a wide band gap *n*-type semiconductor working as an electron conductor coated with dye, a liquid electrolyte for hole conduction, and two transparent conductive electrodes such as conductive indium-tin oxide-coated (**Aldrich Prod. No. 703192**) glass. The photovoltaic process in DSCs begins at the interface between the semiconductor and dye. The electrons in the dye are excited by light and are rapidly transferred to the conduction band of the semiconductor. TiO$_2$ is by far the most widely used semiconductor due to its excellent physical and chemical properties. The electrons pass through the external load and transport back to the counter electrode, which is in contact with the liquid electrolyte. The dye is regenerated by the ionic transport of a redox couple in the electrolyte.

In the past 10 years, several TiNT-based DSCs have demonstrated power conversion efficiencies approaching 10%.[4] The uni-dimensional morphology of the nanotubes provides a natural pathway for the conduction of electrons that is not limited by the intergranular scattering prevalent in nanoparticulate titania films. Scattering from crystal grain boundaries cannot be avoided due to the fact the nanotubes are

For questions, product data, or new product suggestions, contact us at **matsci@sial.com**.

79

polycrystalline, thus resulting in similar electron mobilities for both tubes and particulate films.[23] Recombination times in the nanotubes are much improved (by at least one order of magnitude), resulting in superior charge collection efficiency. The electron diffusion length is large enough and the hollow nature of the nanotubes allows for light trapping and overall deeper light penetration. As a result, thicker nanotube layers (up to 100 µm) could be effectively used[24] for enhanced cell efficiency, while nanoparticulate titania layers thicker than 10–20 µm can be detrimental to performance.

TiNTs are being studied for other emerging solar cell concepts. For example, in partnership with industry our group is developing fully solid-state, ultra-low cost metal oxide solar cell[25] prototypes for niche applications. Perovskite cells are also gaining attention exponentially, and a TiNT-based flexible perovskite cell with efficiency of up to 8.3% has been recently demonstrated.[26]

Conclusion

There has been intensive research on anodic titania nanotubes since their first discovery 14 years ago. The number of annual publications on anodic TiNT has been steadily increasing, exceeding 600 in 2012.[4] Numerous applications are envisioned capitalizing on the synergistic combination of desirable material properties of titania and the enhanced active surface area offered by the unique, controlled architecture of nanotubes. This article discussed two of the most promising applications in the energy sector, namely photocatalysis and photovoltaics. Applications in other high-impact fields such as clean technology, biotechnology, and batteries also may become viable once titania nanotubes are available commercially to R&D groups for quick testing and prototyping.

References

(1) Grimes, C. A.; Mor, G. K. *TiO2 Nanotube Arrays: Synthesis, Properties, and Applications*. Springer-Verlag US: **2009**.
(2) Strukov, D. B.; Snider, G. S.; Stewart, D. R.; Williams, R. S. *Nature* **2008**, *453* (7191), 80–83.
(3) Mardare, D.; Hones, P. *Mater. Sci. Eng., B* **1999**, *68* (1), 42–47.
(4) Lee, K.; Mazare, A.; Schmuki, P. *Chem. Rev.* **2014**, *114* (19), 9385–9454.
(5) Panaitescu, E.; Menon, L. Filtering article containing titania nanotubes. WO2014123878 A1, **2014**.
(6) Tang, Y.; Zhang, Y.; Deng, J.; Wei, J.; Tam, H. L.; Chandran, B. K.; Dong, Z.; Chen, Z.; Chen, X. *Adv. Mater.* **2014**, *26* (35), 6111–6118.
(7) Hoyer, P. *Langmuir* **1996**, *12* (6), 1411–1413.
(8) Jung, J. H.; Kobayashi, H.; van Bommel, K. J. C.; Shinkai, S.; Shimizu, T. *Chem. Mater.* **2002**, *14* (4), 1445–1447.
(9) Tian, Z. R.; Voigt, J. A.; Liu, J.; McKenzie, B.; Xu, H. *J. Am. Chem. Soc.* **2003**, *125* (41), 12384–12385.
(10) Li, D.; Xia, Y. *Nano Lett.* **2004**, *4* (5), 933–938.
(11) Chen, X.; Mao, S. S. *Chem. Rev.* **2007**, *107* (7), 2891–2959.
(12) Gong, D.; Grimes, C. A.; Varghese, O. K.; Hu, W. C.; Singh, R. S.; Chen, Z.; Dickey, E. C. *J. Mat. Res.* **2001**, *16* (12), 3331–3334.
(13) O'Sullivan, J. P.; Wood, G. C. The Morphology and Mechanism of Formation of Porous Anodic Films on Aluminium. **1970**; Vol. *317*, 511–543.
(14) Elmoula, M. A.; Panaitescu, E.; Phan, M.; Yin, D.; Richter, C.; Lewis, L. H.; Menon, L. *J. Mater. Chem.* **2009**, *19* (26), 4483–4487.
(15) Richter, C.; Wu, Z.; Panaitescu, E.; Willey, R. J.; Menon, L. *Adv. Mater.* **2007**, *19* (7), 946–948.
(16) Panaitescu, E.; Richter, C.; Menon, L. *J. Electrochem. Soc.* **2008**, *155* (1), E7–E13.
(17) Richter, C.; Panaitescu, E.; Willey, R.; Menon, L. *J. Mater. Res.* **2007**, *22* (06), 1624–1631.
(18) Fujishima, A.; Honda, K. *Nature* **1972**, *238* (5358), 37-38.
(19) Park, J. H.; Kim, S.; Bard, A. J. *Nano Lett.* **2006**, *6* (1), 24–28.
(20) Richter, C.; Jaye, C.; Panaitescu, E.; Fischer, D. A.; Lewis, L. H.; Willey, R. J.; Menon, L. *J. Mater. Chem.* **2009**, *19* (19), 2963–2967.
(21) Albu, S. P.; Ghicov, A.; Macak, J. M.; Hahn, R.; Schmuki, P. *Nano Lett.* **2007**, *7* (5), 1286–1289.
(22) Podporska-Carroll, J.; Panaitescu, E.; Quilty, B.; Wang, L.; Menon, L.; Pillai, S. C. *Appl. Cata.B-Environ.* **2015**, *176–177*, 70–75.
(23) Zhu, K.; Neale, N. R.; Miedaner, A.; Frank, A. J. *Nano Lett.* **2007**, *7* (1), 69–74.
(24) Jennings, J. R.; Ghicov, A.; Peter, L. M.; Schmuki, P.; Walker, A. B. *J. Am. Chem. Soc.* **2008**, *130* (40), 13364–13372.
(25) Richter, C.; Menon, L.; Panaitescu, E. Solar cells containing metal oxides. WO2014127002 A1, **2014**.
(26) Wang, X.; Li, Z.; Xu, W.; Kulkarni, S. A.; Batabyal, S. K.; Zhang, S.; Cao, A.; Wong, L. H. *Nano Energy* **2015**, *11*, 728–735.

Nanomaterials for Energy Applications

For a complete list of available materials, visit aldrich.com/nanopowders.

Nanopowders and Dispersions

Product Name	Description	Purity	Form	Prod. No.
Aluminum oxide	particle size <50 nm (TEM), >40 m²/g (BET)	-	nanopowder	544833-10G 544833-50G
	particle size 30 - 60 nm (TEM)	-	liquid (suspension) nanoparticles	642991-100ML
	particle size <50 nm (DLS)	-	nanoparticles	702129-100G 702129-500G
Cerium iron oxide hydroxide	<5 nm (DLS)	-	dispersion	796107-100ML
Cerium oxide	<5 nm (DLS)	-	dispersion	796085-100ML
	particle size <5 nm (DLS)	99.5% trace metals basis	dispersion	796077-100ML
Copper	<100 nm (BET)	99% trace metals basis	nanopowder	794317-25G 794317-100G
Indium tin oxide	particle size <50 nm, surface area 27 m²/g	-	nanopowder	544876-5G 544876-25G
	particle size <100 nm (DLS)	-	dispersion	700460-25G 700460-100G
Iron	particle size 35 - 45 nm	99.5% trace metals basis	nanopowder	746843-5G
	avg. part. size 25 nm	99.5% trace metals basis	nanopowder	746827-5G
	avg. part. size 25 nm	99.5% trace metals basis	nanopowder	746835-5G
	particle size 60 - 80 nm	≥99% trace metals basis	nanopowder	746878-25G
	particle size 40 - 60 nm	99% trace metals basis	nanopowder	746851-25G
Iron oxide hydroxide	<5 nm (DLS)	99.5% trace metals basis	dispersion	796093-100ML
ITO	30 nm (SEM)	-	nanopowder	790346-5G

Product Name	Description	Purity	Form	Prod. No.
Platinum	particle size <50 nm (TEM), spec. surface area 98.0 m²/g (BET)	-	nanopowder	685453-100MG 685453-250MG
	particle size 200 nm (SEM)	99.9%, metals basis	nanopowder	771937-250MG
	particle size 3 nm	99.99% trace metals basis	dispersion nanoparticle	773875-25ML
Silicon	<100 nm (BET)	-	nanopowder solid	795585-100G 795585-25G
Titanium	particle size <100 nm	98.5% trace metals basis	dispersion nanoparticles	513415-5G
Titanium(IV) oxide, anatase	particle size <25 nm, spec. surface area 45-55 m²/g	99.7% trace metals basis	nanopowder	637254-50G 637254-100G 637254-500G
Titanium(IV) oxide, brookite	<100 nm	99.99% trace metals basis	nanopowder	791326-5G
Titanium silicon oxide	particle size <50 nm (BET)	99.8% trace metals basis	nanopowder	641731-10G 641731-50G
Zinc	particle size <50 nm, BET surf. area 35-50	≥99% trace metals basis	nanopowder	578002-5G
Zinc iron oxide	particle size <100 nm (BET)	>99% trace metals basis	nanopowder	633844-10G
Zinc oxide	particle size <100 nm, surface area 15-25 m²/g	~80% Zn basis	nanopowder	544906-10G 544906-50G
	particle size <50 nm (BET), >10.8 m²/g	>97%	nanopowder	677450-5G
	avg. part. size <35 nm (APS) particle size <100 nm (DLS)	-	nanoparticles	721077-100G
	avg. part. size <35 nm (APS) particle size <130 nm (DLS)	-	nanoparticles	721085-100G
	avg. part. size <35 nm (APS) particle size <110 nm (DLS)	-	nanoparticles	721093-100G
Zinc titanate	particle size <100 nm (BET)	99% trace metals basis	nanopowder	634409-25G

Metal and Ceramic Nanostructures

Product Name	Description	Form	Prod. No.
Aluminum oxide	diam. × L <20 nm × <100 μm	nanofiber	790915-25G
	diam. × L 2-6 × 200-400 nm	nanowires	551643-10G 551643-50G
	diam. × L <20 nm × <500 μm, 120-150 m²/g (Surface dimension,BET)	nanofiber	790923-25G
Boron nitride	~5 nm (nanotube diameter), surface area >100 m²/g (BET)	nanotubes	802824-1G 802824-250MG
Copper	-	dispersion nanowires	771678-25ML
Copper(II) oxide	diam. × L 10-12 × 75-100 nm, surface area 60-100 m²/g	nanotubes	792004-5G
Gold	diam. × L 30 × 4,500 nm	dispersion (H₂O) nanowires	716944-10ML
	diam. × L 30 × 6,000 nm	dispersion (H₂O)	716952-10ML
	diam. × L 25 × 75 nm, diameter 25 nm 73 nm (long)	colloidal suspension nanorods	716928-10ML
	diam. × L 25 × 75 nm, diameter 25 nm	colloidal suspension dispersion in H₂O	716936-10ML
Manganese(IV) oxide	diam. × L 5-30 × 80-100 nm	nanorod	775711-5G
Nickel(II) oxide	diam. × L ~20 nm × ~10 μm	nanowires	774545-500MG
Silicon carbide	D <2.5 μm	nanofiber	776742-25G
Silver	diam. × L 115 nm × 20-50 μm	liquid (suspension) nanowires	739448-25ML
	diam. × L 60 nm × 10 μm	liquid (suspension) nanowires	739421-25ML
	diam. × L 120-150 nm × 20-50 μm	liquid (suspension) nanowires	778095-25ML
Titanium dioxide	average diameter 25 nm	nanotubes powder	799289-500MG
Titanium(IV) oxide	diam. × L ~100 nm × ~10 μm	nanowires	774510-500MG
	diam. × L ~10 nm × ~10 μm	nanowires	774529-500MG
Tungsten(VI) oxide	diam. × L ~50 nm × ~10 μm	nanowires	774537-500MG
Zinc oxide	diam. × L 90 nm × 1 μm	nanowires	773999-500MG
	diam. × L 50 × 300 nm	nanowires	773980-500MG
	diam. × L 300 nm × 4-5 μm	nanowires	774006-500MG

For questions, product data, or new product suggestions, contact us at matsci@sial.com.

81

MOLYBDENUM DISULFIDE:
UNDERSTANDING HYDROGEN EVOLUTION CATALYSIS

Linyou Cao
Department of Materials Science and Engineering
Department of Physics
North Carolina State University, Raleigh, NC, USA
Email: lcao2@ncsu.edu

Introduction

The production of hydrogen by catalytic water splitting is important for a wide range of industries including renewable energy petroleum refining and for the production of methanol and ammonia in the chemical industry. Within the renewable energy field, hydrogen is an attractive candidate for the storage of energy produced by intermittent renewable energy sources such as solar and wind. Hydrogen is an important chemical feedstock for refining petroleum to produce methanol and ammonia. Within the chemical industry, hydrogen produced from catalytic water splitting has a higher purity and a lower environmental impact than that produced by steam-methane reforming, currently the most common process used for hydrogen production. Despite its significant potential, the widespread adoption of catalytic water splitting has been delayed due to a lack of ideal catalysts with high performance and low cost.

Platinum (Pt) (**Aldrich Prod. No.** 685453) is the most widely used catalyst for the hydrogen evolution reaction (HER) in water. It shows excellent catalytic performance but is much too costly for the mass production of hydrogen. Molybdenum sulfide, an earth abundant metal dichalcogenide, is considered a promising alternative.[1–3] Various molybdenum sulfide materials with different composition (molybdenum disulfide (MoS_2; **Aldrich Prod. No.** 234842) or trisulfide) and morphology (such as nanoparticles, nanotubes, amorphous, or single crystalline MoS_2) have been examined as catalysts for the HER. While significant progress has been achieved, molybdenum sulfide materials are still less effective catalysts than Pt. More effort is necessary to improve their performance to make them a useful HER catalyst for practical applications.

A limited understanding of the catalytic reaction currently constrains development of a high-performance molybdenum sulfide HER catalyst. Catalytic performance is indicated by three main material parameters:

exchange current density (turnover frequency), Tafel slope, and stability. The development of an ideal catalyst requires synergistic optimization to achieve high exchange current density, low Tafel slope, and high stability. However, the understanding of how each of these parameters depends on the physical features of molybdenum sulfide materials continues to be elusive. For instance, it has been widely believed that the edge sites of molybdenum disulfide (MoS_2) are catalytically active and the exchange current density is linearly dependent on the number of edge sites,[4] but recent studies have suggested that the electrical conductivity of the materials also plays an important role in the exchange current density.[5–8]

This article reviews the latest progress in understanding of the catalytic HER at MoS_2. In particular, the new understanding on how the three key parameters (exchange current density, Tafel slope, and stability) depend on the compositional and structural features of molybdenum sulfide materials is presented. We also provide perspectives on the rational design toward the development of high-performance and cost-effective HER catalysts.

Exchange Current Density: Edge Sites and Electrical Conductivity

Exchange current density represents the rate of the catalytic reaction under thermodynamic equilibrium. Conventional wisdom states that the edge site plays an overwhelmingly important role in the catalytic performance and the exchange current density is linearly dependent on the number of edge sites.[4,9] This notion is primarily based on theoretical simulations demonstrating the free energy of the adsorption of hydrogen atoms at the edge site is small;[10] as well as experimental results that show that the exchange current density is dependent on the length of the edge instead of the area of the catalyst materials.[4] However, our recent studies have indicated this well-accepted notion overlooks the important role of electrical conductivity in the exchange current density.[8]

Examination of the catalytic performance of two different types of MoS_2 materials with different numbers of edge sites found that the exchange current density is strongly dependent on the electrical conductivity of the materials, rather than the number of edge sites. One material is a continuous, uniform, and atomically thin MoS_2 film with controlled layer numbers (**Figure 1A–B**), where we confirmed no substantial amount of edge sites. The other is a triangular MoS_2 pyramid platelet (**Figure 1C–D**). The platelet is formed by dislocation-driven growth and its surface is fully covered by edge sites. Both the film and the platelet are synthesized using similar chemical vapor deposition (CVD) processes under

identical temperatures (850 °C) and are expected to have comparable crystallinity.[8,11] In stark contrast with the well-accepted notion, the platelet structure, which is expected to have higher exchange current densities due to the larger number of edge sites, shows an order of magnitude lower value than that of monolayer MoS_2 (**Figure 1E–F**). Additionally, the exchange current densities of the film and the platelet both substantially decrease with increasing thickness. On the other hand, the Tafel slope does not show much variation between the two materials or with the change of layer numbers.
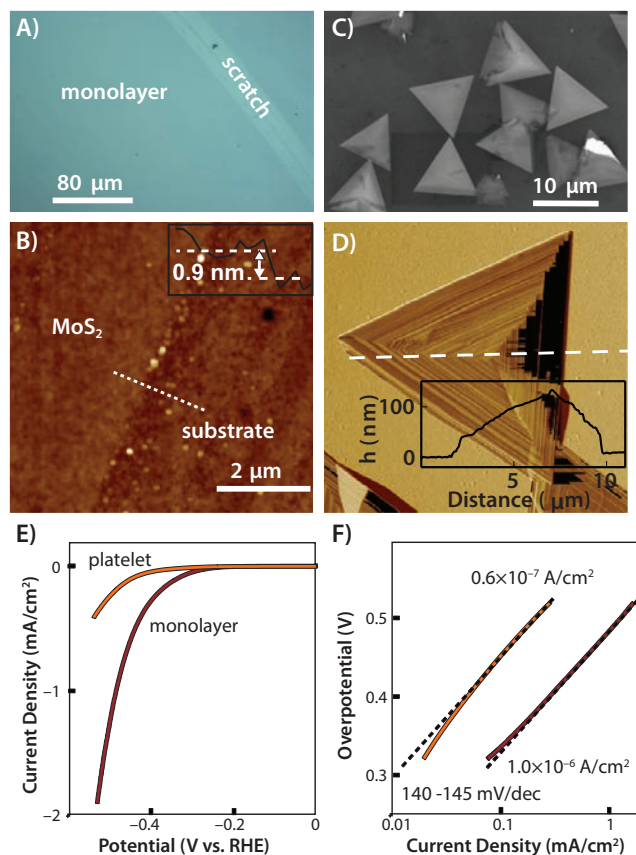
Figure 1. Catalytic performance of MoS_2 monolayer films and pyramid platelets. **A)** Optical image and **B)** AFM image of a monolayer MoS_2 film on glass carbon substrates. A scratch is intentionally introduced to show the contrast between the substrate and the film and for the convenience of characterizing the height of the film. The inset of **B)** is a typical height profile of the film. **C)** AFM image and **D)** SEM image of typical pyramid platelets on glass carbon substrates. The inset of **C)** shows a typical height profile for the platelet. **E)** Polarization curve and **F)** Tafel plot of the MoS_2 monolayer film and pyramid platelets. The Tafel slope and exchange current density are given in **F)** as shown. Adapted from Reference 8. Copyright 2010 American Chemical Society.

The experimental results indicate the electrical conductivity of MoS_2 materials plays an important role in the exchange current density. The results obtained on MoS_2 films are used to illustrate this notion. The exchange current density of the film decreases by 4.45 times with the addition of every new layer (**Figure 2A–B**). This can be explained by the layer dependence of the electrical conductivity. As shown in **Figure 2C**, the electron must transfer from the electrode to the surface in order to drive the catalytic reaction at the surface of MoS_2. The charge transfer in the vertical direction of the MoS_2 material occurs through tunneling,

due to the presence of a van der Waals gap.[12] We can correlate the layer-dependent exchange current density to the efficiency of the electron tunneling, which is expected to decrease with the increasing number of layers and can, therefore, derive the potential barrier in the interlayer gap to be $V_o = 0.119$ V. This result is consistent with the theoretical studies, which predicts the interlayer potential barrier of MoS_2 to be 0.123 V.[13]
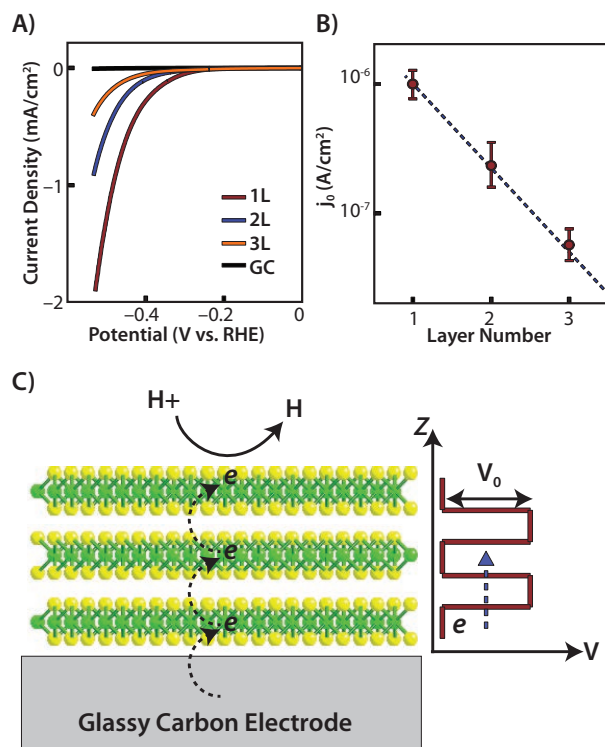
Figure 2. Layer dependence of the catalytic activities of MoS_2 films. **A)** Polarization curves of the synthesized monolayer (red, 1L), bilayer (blue, 2L), and trilayer (orange, 3L) MoS_2 films. The curve of bare glass carbon substrates is also given (black). **B)** The exchange current density of the MoS_2 film as a function of the layer number. The current density is plotted in a logarithmic scale. The dashed line is a fitting of $\log y = -0.65x - 5.35$. **C)** Schematic for the hopping of electrons in the vertical direction of MoS_2 layers. The right side illustrates the potential barrier in the interlayer gap. Adapted from Reference 8. Copyright 2010 American Chemical Society.

The electrocatalytic reaction involves a two charge transfer processes, in which (1) electrons from the surface of the catalyst flow to the proton in the electrolyte solution, which may give rise to hydrogen atoms adsorbed on the surface as intermediate products, and (2) electrons from the electrode (glassy carbon) underneath the catalyst flow to the surface of the catalyst. Under thermodynamic equilibrium, the exchange current density essentially represents the overall charge transfer rate from the electrode to the proton. The role of the active site is to facilitate the first charge transfer by enabling a small free energy of adsorption for hydrogen atoms. Previous theoretical studies have demonstrated that the rate of the first charge transfer is the highest when the free energy of adsorption is close to zero.[10,14] In contrast, the electrical conductivity may affect the rate of the second charge transfer as just discussed. It should be pointed out that the effect of electrical conductivity on the charge transfer rate is different from the potential drop caused by the electrical resistance of catalyst materials and the latter may be eliminated by performing *iR* correction.

According to this understanding, the exchange current density can be improved either by increasing the number of active sites, which has been the major strategy used to date, or by increasing the conductivity of the materials. Many recent studies have demonstrated an improvement in the catalytic performance of MoS_2 as the result of improved electrical conductivity. In fact, a significant improvement in the catalytic performance has been reported by changing the crystalline phase of MoS_2 from 2H to 1T. The 1T phase is known to be more conductive than the 2H phase.[5–7] Additionally, cobalt and nickel doped MoS_2 show improved catalytic performance,[15] which could be ascribed to the improvement in electrical conductivity as well. As a result of the difference in electrical conductivity, crystalline molybdenum sulfide materials can enable much higher exchange current densities than amorphous counterparts (see **Figure 3D**).[16]

Tafel Slope: Disorder in Crystallinity

Tafel slope indicates the dependence of the catalytic reaction rate on applied overpotentials. The lower the Tafel slope, the faster the reaction rate increases with applied overpotentials. Generally, the Tafel slope (η) of an electrochemical reaction is dictated by the rate-determining step of the reaction and can be written as a function of the number of electrons involved (z) and the charge transfer coefficient (a) of the rate-determining step as $\eta = 2.3zRT/aF$,[14,17] where R is the ideal gas constant, T is the absolute temperature, and F is the Faraday constant. For the HER of molybdenum sulfide materials, which usually occurs in acid media, there are three reaction steps that could be involved:

(1) the primary discharge step (Volmer reaction):

$$H_3O+ + e- \rightarrow H_{ads} + H_2O$$
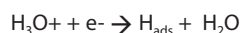
(2) an electrochemical desorption step (Heyrovsky reaction):

$$H_{ads} + H_3O+ + e- \rightarrow H_2 + H_2O$$
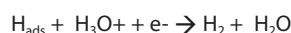
(3) a recombination step (Tafel reaction):

$$H_{ads} + H_{ads} \rightarrow H_2$$

It is well known that the Tafel slope of the HER would be different depending on which reaction is the rate-determining step because each of the reactions has a different charge transfer coefficient (a). More specifically, the Tafel slope would be 120 mV/decade, 40 mV/decade, and 30 mV/decade when the rate-determining step is reaction (1), (2), and (3), respectively. The Tafel slope may also be another value if the rate-determining step involves more than one of the three reactions. The Tafel slope of the HER at molybdenum sulfide reported in the literature shows broad variation in the range of 40–140 mV/decade.[4–6,15–29] This indicates the rate-determining step involved may vary substantially, but how the rate-determining steps depend on the physical features of the materials is essentially unexplored.

The crystallinity of molybdenum sulfide materials may affect the Tafel slope.[16] We examined the HER at molybdenum sulfide films with different crystallinity, including single crystalline, polycrystalline, and amorphous with inclusion of some fewlayer nanocrystals in lateral size of 4–5 nm (**Figure 3**). The crystallinity control was achieved by regulating the growth temperature (**Figure 3B**). **Figure 3C** shows the Tafel slope has a strong dependence on the crystallinity. For the molybdenum sulfide materials with low crystallinity (amorphous or amorphous with inclusion of tiny nanocrystals) the Tafel slope is as low as 40 meV/decade. It increases up to 60 meV/decade and 80–90 meV/decade for polycrystalline and single crystalline materials, respectively.
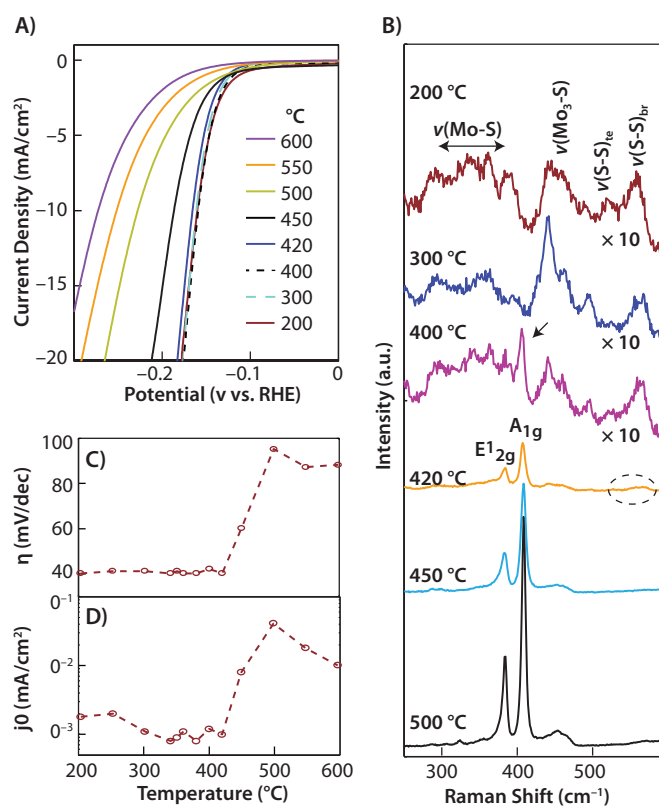
Figure 3. Dependence of the catalytic performance on the crystallinity of molybdenum sulfide materials. **A)** Polarization curves of the molybdenum sulfide materials grown at different temperatures. The growth temperatures are labeled as shown. **B)** Raman spectra of the molybdenum sulfide materials grown at different temperatures. The growth temperature and assignment of the Raman peaks are given in the figure. For visual convenience, the intensities of the Raman spectra of the materials grown at 400 °C or lower temperatures are multiplied by a constant of 10. The arrow indicates the Raman peak of crystalline MoS_2 in the materials grown at 400 °C, and the dashed circle indicates the Raman peaks of MoS_3 in the materials grown at 420 °C. **C)** Tafel slopes and **D)** exchange current densities of the molybdenum sulfide materials as a function of the growth temperature. Adapted from Reference 16. Copyright 2010 American Chemical Society.

The low Tafel slope (40 meV/decade) of the materials with low crystallinity is likely due to the presence of certain types of defects. These defects could serve as active sites at which the rate-determining step of the catalytic reaction is the electrochemical desorption step. While more studies are necessary to better understand the nature of these defects, we believe one of them is a disulfur complex (S_2^{2-}). Molybdenum trisulfide, in which the sulfur is mainly in the form of disulfur complex, always shows a Tafel slope of 40 meV/decade.[16] The disulfur complex might also exist in amorphous molybdenum disulfide materials due to the structural disorder.

The association of low Tafel slopes with low crystallinity (amorphous or tiny nanocrystals) is supported by results from other groups. Similar low Tafel slopes (40 meV/decade) have been reported in nanocrystalline MoS_2 with few layers, in lateral size of <10 nm and phase-engineered MoS_2 nanosheets that are expected to include many defects.[6,7,17] Other groups have also reported that the molybdenum sulfide materials with disulfur complexes (S_2^{2-}), such as MoS_3 or thiomolybdate with MoS_3-like structures, or $Mo_3S_{13}^{2-}$ clusters, all show Tafel slopes of 40 mV/decade.[23,30] Recent reports show the Tafel slope of MoS_2 nanosheets can be substantially lowered by intentionally introducing defects via controlled oxidation.[16,28]

Stability: Oxidation!

Stability is an indicator of how long the catalytic performance can be maintained. Molybdenum sulfide's catalytic performance substantially degrades with reaction time. However, an understanding of the underlying mechanism of this degradation is very limited.

Degradation in the catalytic activity of molybdenum sulfide can be ascribed to the loss of catalytically active sites.[16] **Figure 4A** shows the polarization curves and corresponding Tafel plots collected from the material grown at 300 °C at different reaction times (different cycles). The exchange current density obviously decreases with the reaction time while the Tafel slope remains constant. In addition, the capacitance (which indicates the surface area of the material) decreases in conjugation with the exchange current density and the turnover frequency. This is an indicator that charge transfer efficiency at each site remains essentially unchanged.[16] Therefore, the observed degradation in the catalytic activity can be attributed to the decrease in the number of active sites.

The loss of catalytic active sites results from the oxidation of the materials. To better understand this phenomenon, the composition of molybdenum sulfide materials through the catalytic reaction process was monitored by XPS measurements. The oxidation of MoS_2 can be clearly seen as evidenced by the appearance of higher oxidation states of Mo (Mo^{6+} and Mo^{5+}) after the catalytic reaction.[16] The oxidation is caused by the oxygen in the ambient environment rather than the applied overpotential because the applied potential is too low (< +0.2 V vs. RHE) to oxidize MoS_2. The volume of the catalyst materials decrease after the catalytic reaction, which lends further evidence of oxidation.[16] This is because the molybdenum oxide resulting from the oxidation is weakly soluble in aqueous solution and may be gradually dissolved.

It is believed the stability of molybdenum sulfide increases with the crystallinity because the material with high crystallinity resists oxidation better. **Figure 4** shows the polarization curve extracted from the cyclic voltammetry measurement of molybdenum sulfide materials grown at 300 °C, 420 °C, and 450 °C. The crystallinity of the materials is known to increase with the growth temperature. The materials grown at 300 °C, which mainly consist of amorphous material, show a decrease in cathodic current after ~250 cycles. In contrast, the material grown at 420 °C that involves a substantial amount of nanocrystalline MoS_2 maintains the current for up to ~1,000 cycles. The materials grown at 450 °C or higher temperatures, which are of higher crystalline quality, are even more stable—showing constant currents for thousands of cycles.

Conclusion and Outlook

The improved understanding of the correlation of the three main parameters (exchange current density, Tafel slope, and stability) with the compositional and structural physical features of molybdenum sulfide may provide useful guidance for the rational design of high-performance and low-cost HER catalysts. It indicates the electrical conductivity, active sites, and crystallinity must be synergistically optimized in order to obtain optimal catalytic performance with high exchange current density, low Tafel slope, and high stability. The optimization of the electrical conductivity and crystallinity can serve to improve the exchange current density and stability, respectively. It may be readily achieved by simply decreasing the number of layers and increasing growth temperatures. However, optimization of the active sites is more challenging. This includes increasing the number of active sites and controlling their chemical nature. The control of the chemical nature of active sites is complicated because it is necessary to balance between the effect of active sites on both exchange current density and Tafel slope. The nature of active sites may dictate the free energy of adsorption and the rate-determining step. Ideal active sites should have small (close to zero) free energy of adsorption and could enable either the Heyrovsky or Tafel reaction to be the rate-determining step.

A rational design of the ideal active sites requires better understanding for the following questions:

- What other sites of molybdenum sulfide could be catalytically active except the edge site?

- How could the free energy of adsorption and rate-determining step vary with the different active sites?

- How would the chemical nature of active sites depend on the compositional/physical features (such as dopant) of the materials?

More studies are necessary because the current understanding of these questions is very limited.

Figure 4. Dependence of the catalytic stability of molybdenum sulfide on the growth temperature. Polarization curves of the molybdenum sulfide materials grown at **A**) 300 °C, **B**) 420 °C, and **C**) 450 °C with different cycles. The insets are corresponding Tafel plots in which only the results for the 1st and 2,000th cycle are given for visual convenience. Reprinted with permission from Reference 16. Copyright 2010 American Chemical Society.

For questions, product data, or new product suggestions, contact us at **matsci@sial.com**.

85

References

(1) Benck, J. D.; Hellstern, T. R.; Kibsgaard, J.; Chakthranont, P.; Jaramillo, T. F. *ACS Catalysis* 2014, *4*, 3957.

(2) Bonde, J.; Moses, P. G.; Jaramillo, T. F.; Norskov, J. K.; Chorkendorff, I. *Faraday Discuss* 2008, *140*, 219.

(3) Laursen, A. B.; Kegnaes, S.; Dahl, S.; Chorkendorff, I. *Energ Environ Sci* 2012, *5*, 5577.

(4) Jaramillo, T. F.; Jorgensen, K. P.; Bonde, J.; Nielsen, J. H.; Horch, S.; Chorkendorff, I. *Science* 2007, *317*, 100.

(5) Lukowski, M. A.; Daniel, A. S.; Meng, F.; Forticaux, A.; Li, L.; Jin, S. *J. Am. Chem. Soc.* 2013, *135*, 10274.

(6) Voiry, D.; Salehi, M.; Silva, R.; Fujita, T.; Chen, M. W.; Asefa, T.; Shenoy, V. B.; Eda, G.; Chhowalla, M. *Nano Lett.* 2013, *13*, 6222.

(7) Wang, H.; Lu, Z.; Xu, S.; Kong, D.; Cha, J. J.; Zheng, G.; Hsu, P.-C.; Yanb, K.; Bradshaw, D.; Prinz, F. B.; Cui, Y. *Proc. Natl. Acad. Sci. USA* 2013, *110*, 19701.

(8) Yu, Y.; Huang, S.-Y.; Li, Y.; Steinmann, S. N.; Yang, W.; Cao, L. *Nano Lett.* 2014, *14*, 553.

(9) Tsai, C.; Abild-Pedersen, F.; Nørskov, J. K. *Nano Lett.* 2014, *14*, 1381.

(10) Greeley, J.; Jaramillo, T. F.; Bonde, J.; Chorkendorff, I.; Nørskov, J. K. *Nat. Mater.* 2006, *5*, 909

(11) Yu, Y. F.; Li, C.; Liu, Y.; Su, L. Q.; Zhang, Y.; Cao, L. Y. *Sci Rep-Uk* 2013, *3*.

(12) Tang, H.; Morrison, S. R. *Thin Solid Films* 1993, *227*, 90.

(13) Cappelluti, E.; Roldan, R.; Silva-Guillen, J. A.; Ordejon, P.; Guinea, F. *arXiv: 1304.4831* 2013.

(14) Parsons, R. *Trans. Faraday Soc.* 1958, *54*, 1053.

(15) Merki, D.; Hu, X. L. *Energ Environ Sci* 2011, *4*, 3878.

(16) Yanpeng Li; Yifei Yu; Huang, S.-Y.; Huang, Y.; Nielsen, R. A.; III, W. A. G.; Li, Y.; Cao, L. *ACS Catalysis* 2015, *5*, 448.

(17) Li, Y. G.; Wang, H. L.; Xie, L. M.; Liang, Y. Y.; Hong, G. S.; Dai, H. J. *J Am Chem Soc* 2011, *133*, 7296.

(18) Chang, Y. H.; Lin, C. T.; Chen, T. Y.; Hsu, C. L.; Lee, Y. H.; Zhang, W. J.; Wei, K. H.; Li, L. J. *Adv Mater* 2013, *25*, 756.

(19) Deng, J.; Yuan, W. T.; Ren, P. J.; Wang, Y.; Deng, D. H.; Zhang, Z.; Bao, X. H. *Rsc Adv* 2014, *4*, 34733.

(20) Faber, M. S.; Dziedzic, R.; Lukowski, M. A.; Kaiser, N. S.; Ding, Q.; Jin, S. *J. Am. Chem. Soc.* 2014, DOI: 10.1021/ja504099w.

(21) Ge, X.; Chen, L.; Zhang, L.; Wen, Y.; Hirata, A.; Chen, M. *Adv. Mater.* 2014, *26*, 3100.

(22) Huang, X.; Zeng, Z.; Bao, S.; Wang, M.; Qi, X.; Fan, Z.; Zhang, H. *Nature Communications* 2013, *4*, 1444.

(23) Kibsgaard, J.; Jaramillo, T. F.; Besenbacher, F. *Nat Chem* 2014, *6*, 248.

(24) Kong, D.; Wang, H.; Lu, Z.; Cui, Y. *J. Am. Chem. Soc.* 2014, *136*, 4897.

(25) Liao, L.; Zhu, J.; Bian, X. J.; Zhu, L. N.; Scanlon, M. D.; Girault, H. H.; Liu, B. H. *Adv Funct Mater* 2013, *23*, 5326.

(26) Merki, D.; Fierro, S.; Vrubel, H.; Hu, X. L. *Chem Sci* 2011, *2*, 1262.

(27) Vrubel, H.; Hu, X. L. *Acs Catalysis* 2013, *3*, 2002.

(28) Xie, J. F.; Zhang, J. J.; Li, S.; Grote, F.; Zhang, X. D.; Zhang, H.; Wang, R. X.; Lei, Y.; Pan, B. C.; Xie, Y. *J Am Chem Soc* 2013, *135*, 17881.

(29) Yan, Y.; Xia, B.; Qi, X.; Wang, H.; Xu, R.; Wang, J.-Y.; Zhang, H.; Wang, X. *Chem. Commun.* 2013, *49*, 4884.

(30) Vrubel, H.; Merki, D.; Hu, X. L. *Energ Environ Sci* 2012, *5*, 6136.

Precursors for 2D Materials

For a complete list of available materials, visit aldrich.com/periodic.

Product Name	Form	Particle Size	Purity	Prod. No.
Boron nitride	powder	~1 µm	98%	255475-50G 255475-250G
	nanopowder	avg. part. size <150 nm (BET)	99% trace metals basis	790532-10G
Manganese(IV) oxide	powder and chunks	-	≥99.99% trace metals basis	529664-5G 529664-25G
Molybdenum(VI) oxide	powder	-	99.98% trace metals basis	203815-5G 203815-25G
	nanopowder	100 nm (TEM)	99.5% trace metals basis	775703-5G
Molybdenum(IV) selenide	powder	-325 mesh	99.9% trace metals basis	778087-5G
Molybdenum(IV) sulfide	powder	~6 µm (max. 40 µm)	-	69860-100G 69860-500G
	powder	<2 µm	99%	234842-100G 234842-500G
	nanopowder	particle size 90 nm (APS)	99% trace metals basis	804169-10G
Tungsten(VI) oxide	nanopowder	particle size <100 nm (TEM)	-	550086-5G 550086-25G
	powder	-	99.995% trace metals basis	204781-10G 204781-50G 204781-250G
Tungsten(IV) sulfide	powder	2 µm	99%	243639-50G
	nanopowder	avg. part. size 90 nm (SEM)	99% trace metals basis	790583-5G

Graphene Oxide and Reduced Graphene Oxide

For a complete list of available materials, visit aldrich.com/graphene.

Product Name	Description	Form	Prod. No.
Graphene oxide	2 mg/mL	dispersion in H_2O	763705-25ML 763705-100ML
	Dispersibility: Polar solvents Monolayer content (measured in 0.5mg/mL): >95%, 4 mg/mL	dispersion in H_2O	777676-50ML 777676-200ML
	15-20 sheets, 4-10% edge-oxidized, 1 mg/mL	dispersion in H_2O	794341-50ML 794341-200ML
	sheets	flakes	763713-250MG 763713-1G
	15-20 sheets 4-10% edge-oxidized	powder	796034-1G
	4 cm (diameter) x 12-15mm (thickness), non-conductive	film	798991-1EA
Graphene Oxide Nanocolloids	2 mg/mL	dispersion in H_2O	795534-50ML 795534-200ML
Graphene oxide, ammonia functionalized	1 mg/mL	dispersion in H_2O	791520-25ML 791520-100ML
Reduced graphene oxide	chemically reduced	powder	777684-250MG 777684-500MG

Graphene

For a complete list of available materials, visit aldrich.com/graphene.

Graphene and Graphene Nanoplatelets

Product Name	Form	Sheet Resistance (Ω/sq)	Prod. No.
Graphene dispersion	10 mg/mL, dispersion (in NMP)	<10^3 (graphene)	803839-5ML
Graphene nanoplatelets	Black powder	10 (+/-5) (for a 25 μm film)	799084-500MG
Graphene nanoplatelets	1 mg/mL, dispersion in H$_2$O	10 (+/-5) (for a 25 μm film)	799092-50ML

Graphene Nanoribbons

Product Name	Purity	Dimension	Surface Area	Prod. No.
Graphene nanoribbons	≥90.0% carbon basis, TGA	L × W 2-15 μm × 40-250 nm	BET surf. area 48-58 m^2/g	797774-500MG
Graphene nanoribbons, alkyl functionalized	≥85% carbon basis, TGA	L × W 2-15 μm × 40-250 nm	BET surf. area 38 m^2/g	797766-500MG

Graphene Inks

Product Name	Description	Prod. No.
Graphene dispersion	with ethyl cellulose in cyclohexanone and terpineol, inkjet printable	793663-5ML
	with ethyl cellulose in terpineol, gravure printable	796115-10ML
	with ethyl cellulose in terpineol, screen printable	798983-10ML

Graphene Films

Product Name	Sheet Resistance (Ω/sq)	Prod. No.
Monolayer graphene film, 1 cm x 1 cm on copper foil	600	773697-4EA
Monolayer graphene film, 1 in x 1 in on copper foil	350	799009-1EA
Monolayer graphene film, 1 cm x 1 cm on quartz	600	773719-4EA
Monolayer graphene film, 1 cm x 1 cm on SiO$_2$/Si substrate	600	773700-4EA
Monolayer graphene film, 1 in. x 1 in. on PET film	700	745863-1EA 745863-5EA
Monolayer graphene film, 2 in. x 2 in. on PET film	700	745871-1EA
Suspended monolayer graphene on TEM grid substrate (Quantifoil gold)	170	798177-1PK

HAVE YOU MISSED A RECENT ISSUE?

- Vol. 10 No. 2: Graphene and Carbon Materials (ROM)
- Vol. 10 No. 1: 10th Anniversary Issue—Materials that Matter (RJQ)
- Vol. 9 No. 4: Materials for Energy Harvesting and Storage (REO)
- Vol. 9 No. 3: Polymers in Therapeutics and Nanomedicine (QZP)
- Vol. 9 No. 2: Inorganic Materials in Biomedical Applications (QIV)
- Vol. 9 No. 1: Materials for Flexible and Printed Electronics (QFD)

To view a complete library of issues or to subscribe to our newsletter, visit

aldrich.com/materialmatters

PERFLUOROSULFONIC ACID MEMBRANES
FOR FUEL CELL AND ELECTROLYSER APPLICATIONS

Deborah Jones
Institut Charles Gerhardt
CNRS–University of Montpellier, 34090 Montpellier, France
Email: Deborah.Jones@univ-montp2.fr

Introduction

Advances in the electrochemical conversion of water to and from hydrogen and oxygen have principally been achieved through the development of new materials and by understanding the mechanisms of the degradation of proton exchange membrane fuel cells (PEMFC) during operation. Electrochemical conversion of hydrogen and oxygen into water in fuel cells relies on a proton exchange membrane (PEM). The same is true for the conversion of water to hydrogen and oxygen through PEM water electrolysers (PEMWE). In both PEMFC and PEMWE, the PEMs form the heart of the electrochemical cells, where they ensure conduction of protons from the anode to the cathode, separation of reactant (fuel cell) or product (electrolyser) gases, and electrical insulation of the electrodes. Many of the requirements for effective PEMs in fuel cells and electrolysers are the same and have long been recognized. However, it is only recently that notable advancements have been made to enable chemically and mechanically stable membranes with high proton conductivity. An extensive library of polymers and ionomers has been developed and evaluated in recent years. This has led to a vast number of novel sulfonic acid functionalized non-fluorinated polyaromatics[1] and polymer materials comprising protogenic functions other than sulfonic acid (typically phosphonic and heterocycle functionalized materials). These endeavors have also notably advanced perfluorosulfonic acid (PFSA) polymer technologies to produce a new generation of state-of-the-art fuel cell membranes.

PFSA Polymer Types

Nafion®, developed by DuPont, is generated by free radical-initiated copolymerization of a perfluorinated vinyl ether sulfonyl fluoride co-monomer with tetrafluoroethylene (TFE). This gives a poly(tetrafluoroethylene) backbone with perfluoroether pendant side chains terminated by sulfonic acid groups (**Figure 1**). Polymers with identical structure such as Flemion®, Aciplex®, and Fumion® F

are produced by Asahi Glass Company, Asahi Kasei, and FuMA-Tech, respectively. With the advent of related perfluorinated ionomers with shorter pendant side chains, the Nafion®-type composition is termed as the "long-side-chain" (LSC) ionomer, which refers to the "long" side chain of the type shown in **Figure 1A**. The equivalent weight (EW) of an ionomer is the weight of the polymer required to provide 1 mole of exchangeable protons, i.e., it is the inverse of the ion exchange capacity (IEC). These properties are directly responsible for several of the key features of PEMs such as proton conductivity and the tendency to swell in water and shrink in low relative humidity. The polymer EW and IEC depend on the ratio of TFE and side-chain functionalized TFE. The long-side-chain membranes typically comprise an ionomer of equivalent weight 1,100–900 g/mole or ion exchange capacity of 0.91–1.11 mmole/g.

A) $— (CF_2CF_2)_m CF_2CF —$
$OCF_2CFOCF_2CF_2SO_3H$
CF_3
Nafion®
EW 1100, m = 6.6

B) $— (CF_2CF_2)_n CF_2CF —$
$OCF_2CF_2SO_3H$
Aquivion®
EW 830, n = 5.5

C) $— (CF_2CF_2)_p CF_2CF —$
$OCF_2CF_2CF_2CF_2SO_3H$
3M™
EW 850, p = 4.7
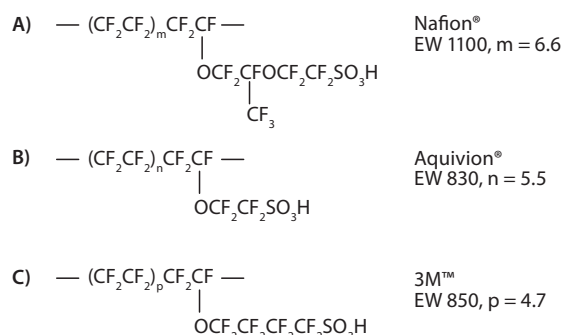
Figure 1. Nafion®, Aquivion®, and 3M™ perfluorinated sulfonic acid ionomer structures

Composition, Structure, and Synthesis Routes

A short-side-chain (SSC) perfluorinated ionomer (the Dow membrane) with no fluoroether group in the pendant side-chain comprising only two CF_2 groups was introduced during the 1980s by the Dow Chemical Company.[2] Although significant improvement in fuel cell performance was obtained by researchers at companies such as Ballard Power Systems, the complexity of the synthesis route to the SSC monomer (**Figure 2**) was probably one of the main obstacles in the industrial development of the corresponding SSC ionomer. Subsequently, Solexis (now known as Solvay Specialty Polymers) applied its fluorovinylether process to the production of the SSC monomer (**Figure 2**) on an industrial scale and launched Hyflon® Ion (known as Aquivion® since 2009, **Figure 1B**).[3]
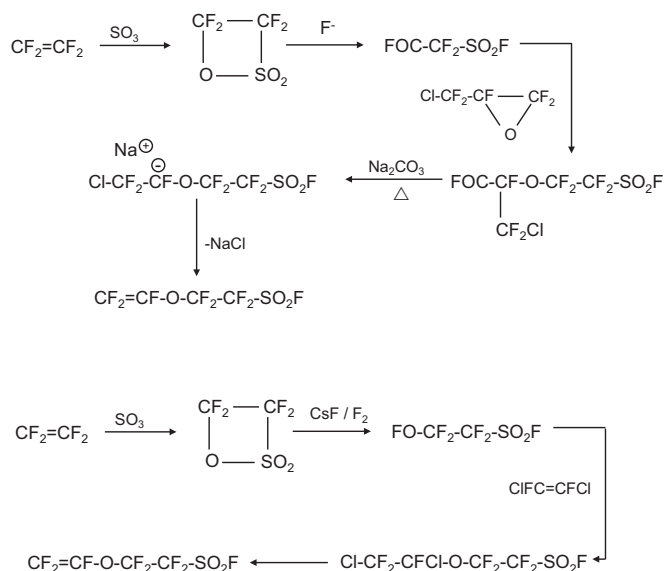
Figure 2. Dow (above) and Solexis (below) routes for the synthesis of the SSC sulfonylfluoridevinylether monomer. Adapted from Reference 32. Copyright 2005 American Chemical Society.

In the same period, the 3M™ Corporation developed an ionomer (the 3M™ ionomer, **Figure 1C**) with a fluoroether-free pendant chain with four –CF_2- groups by the electrochemical fluorination of a hydrocarbon starting material (**Figure 3**).[4] Since the identification of the prevalence of the degradation mechanism resulting from the radical attack on carboxylic acid end-groups of the PFSA backbone leading to so-called "unzipping" of the polymer chains,[5] PFSAs are further stabilized by post-synthesis fluorination.
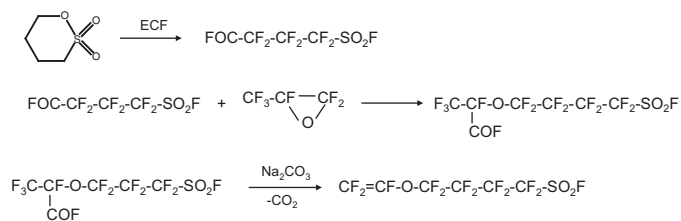
Figure 3. 3M™ route for the synthesis of "medium-side-chain" perfluoro-4-(fluorosulfonyl) butoxylvinyl ether monomer. Adapted from Reference 4.

The compositional and structural differences between LSC and SSC ionomers impart their specific properties. At a given polymer EW, the SSC-type Aquivion® membranes are characterized by a higher heat of fusion than LSC Nafion®-type membranes.[6] Aquivion® retains its semi-crystalline character even at low EW. Further, Aquivion® with an EW of 830 g/mol shows the same heat of fusion characteristic of the most commonly available Nafion® of EW 1,100 g/mlol (**Figure 4**). In addition, both the absence of the pendant CF_3 group and the shorter side chain give a polymer of higher glass transition temperature at a given polymer EW (T_g Nafion® ca. 100 °C, 3M™ ca. 125 °C, and Aquivion® ca. 140 °C), which extends the operating temperature to higher values. Wide angle X-ray scattering (WAXS) shows that the crystallinity decreases with decreasing ionomer EW, which is consistent with a shorter PTFE segment length. For the same EW, the crystallinity is lower in LSC than in SSC ionomers to such an extent that SSC membranes exhibit crystallinity at EWs where LSC ionomers are amorphous. The 3M ionomer of EW 700 shows no crystalline peak,[7] which suggests that a minimum PTFE segment length between adjacent side chains is necessary for the formation of crystalline hydrophobic domains.
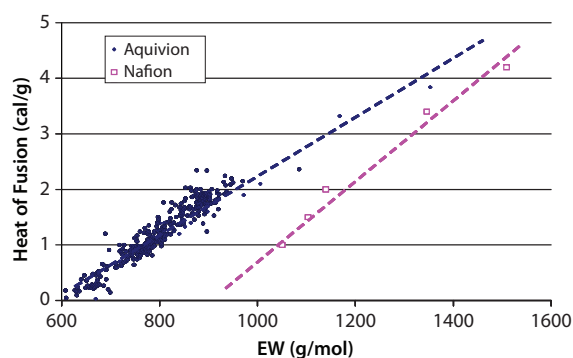
Figure 4. Heat of fusion of Aquivion® and Nafion® ionomers of various polymer equivalent weights.(Figure provided by Solvay Speciality Polymers.) Data for Nafion® adapted with permission from Reference 33. Copyright 1989 American Chemical Society.

PFSA Ionomer Dispersions

The dispersion of PFSA ionomers in catalyst inks is a critical factor in determining the activity of catalyst layers in membrane electrode assemblies of PEMFCs and PEMWEs. Nafion® and other PFSAs do not form true solutions in low-boiling alcohols/water.[8] Analysis of small angle X-ray scattering (SAXS) profiles indicates consistent values of 2–2.5 nm for the radius for LSC PFSA dispersed in polar solvents and smaller radii of 1.5–1.7 nm for similar rod-like particles of SSC PFSA. Transmission electron microscopy of LSC membranes shows vermicular structures around 30 nm in length. Despite these observations, dynamic light scattering indicates objects of radius at a different length scale, which is consistent with aggregation into secondary structures. To date, there appears to be no general understanding of the solvent-dependent state of PFSA aggregates and their dispersion.

The morphology and properties of films formed by solvent removal from such dispersions differ greatly from those of the more crystalline form produced by extrusion. High temperature annealing is necessary to induce polymer chain reorganization into semi-crystalline domains. This improves membrane mechanical properties. Aquivion® dispersions of various EW and at various ionomer concentrations are commercialized by Solvay Specialty Polymers (available from Sigma-Aldrich) for use in membrane electrode assembly (MEA) components for membrane casting, catalyst ink development, and gas diffusion layer surface modification.[9]

Conductivity and Water Uptake

Proton conductivity in PFSA membranes depends on the polymer EW (number of charge carriers), hydration number (λ, number of water molecules/sulfonic acid group), polymer structure, membrane morphology, and temperature. All of these factors also affect the proton mobility. The proton conductivity of SSC PFSA membranes of EW 700–1,000 g/mole is displayed in **Figure 5**. The conductivity of 700 EW Aquivion® breaks through the barrier of the 100 mS cm^{-1} at temperatures between 80–110 °C and relative humidity (RH) >60%. The conductivity at 25% RH for the same temperature range is >200 mS cm^{-1}. While water content and proton mobility have a critical impact on proton conductivity, the water retention and permeation phenomena also play a critical role in determining fuel cell performance. Generally, the water uptake measured from the saturated vapor is lower than that from liquid. Thus, SSC Aquivion® membranes exhibit high thermal stability (arising from the increased T_g) and higher proton conductivity even at low relative humidity (enabled by use of lower EW ionomers), making them attractive for high temperature, higher performance PEMFCs and PEMWEs.
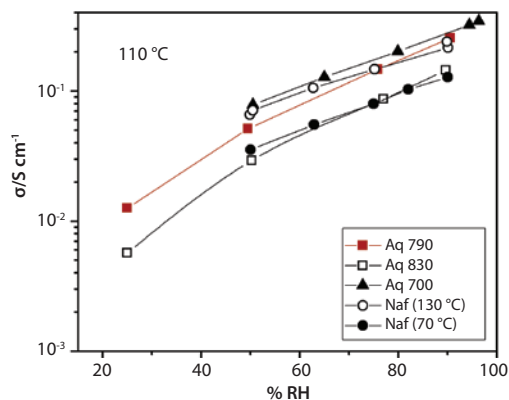
Figure 5. Dependence of proton conductivity at 110 °C of EW 700, 790, and 830 Aquivion®, and of EW 1100 Nafion® at 70 and 130 °C. (Figure provided by Mario Casciola, Università di Perugia, Italy.)

The side chain length of the PFSA impacts water uptake from liquid. For example, as shown in **Figure 6**, water uptake of 35 wt% is obtained with Nafion® EW 1100 and Aquivion® EW 900.
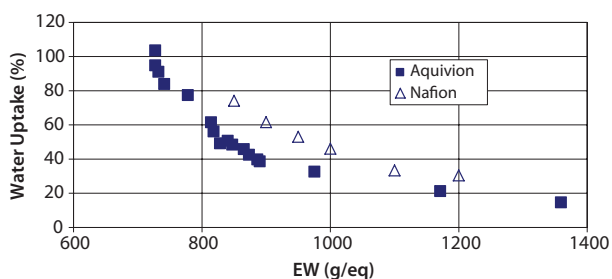
Figure 6. Water uptake from liquid water at 100 °C for extruded Aquivion® and Nafion® membranes as a function of the equivalent weight. Redrawn from Reference 6.

Membrane Durability

Membrane durability is a critical factor impacting fuel cell lifetime. The difference in side chain length and the presence or absence of a pendant perfluoroether group can significantly influence the chemical stability of LSC and SSC membranes. This is especially true in the case of a free radical attack in fuel cell operation conditions where the mechanism implicated in polymer degradation is different from the "unzipping" mechanism mentioned previously. Indeed, unzipping from the polymer chain ends should be reduced in a chemically stabilized PFSA membrane. In *ex situ* degradation studies, the membranes are immersed in Fenton's reagent, which is comprised of aqueous hydrogen peroxide and a ferrous salt and generates radicals. In experiments comparing the fluoride ion released from stabilized and non-stabilized Aquivion® and Nafion®-112 (extruded and cast) after immersion in Fenton's reagent, significantly lower fluoride emission is observed for stabilized extruded Aquivion® than from the non-stabilized material. Further, stabilized Aquivion® and the Nafion® membranes both show similar fluoride release.[10] Solid-state ^{19}F NMR spectroscopy of Nafion®-112 and Aquivion® before and after aging in Fenton's reagent show much less change in relative peak area of the signal from the SCF_2 group of Aquivion® than of Nafion®-112. This shows that the short side chain of Aquivion® is considerably less sensitive to radical attack than the long side chain of Nafion®.[11] Similar conclusions were reached following a spin-trapping-based electron spin resonance *ex situ* study where hydroxyl radicals were generated by UV irradiation of aqueous hydrogen-peroxide-treated 3M™, Aquivion®, and Nafion® membranes.[12] The absence of the $-O-CF_2-CF(CF_3)$- segment in the Aquivion® and 3M™ structures may directly explain their improved side chain stability.

The fluoride emission rate (FER) is one method used to assess PFSA membrane degradation. The FER of a membrane is measured from the exhaust gases that condense at the anode and cathode during *in situ* accelerated aging testing of fuel cells. It has been shown that holding the fuel cell at open circuit voltage (OCV) accelerates chemical degradation of PFSA membranes. Accelerated stress testing (AST) increases the rate of membrane degradation and is performed by maintaining membranes at OCV, high temperature, and intermediate or low relative humidity. In recent investigations comparing the durability of Aquivion® and Nafion® membranes at OCV hold testing at 90 °C and 50% relative humidity in a fuel cell, the anode/cathode FER was measured to be 8×10^{-3} µmol $F.cm^{-2}$ h^{-1} for Aquivion® E79-03S (30 µm membrane) and 0.18 µmol $F.cm^{-2}$ h^{-1} for Nafion®-212 (50 µm membrane), respectively. This shows significantly lower fluoride release from the SSC membrane.[13] These results corroborate the ranking of relative stability to radical attack of long- and short-side-chain PFSA membranes demonstrated by *ex situ* degradation testing.

Better Membranes Through Chemical Modification and Crosslinking

Mechanical degradation of membranes is directly related to macroscopic swelling and contraction of the membrane. Membrane swelling is accompanied by high water uptake, which can be difficult to eliminate, as well as increased plasticity and softening, which generally occurs in membranes that have the high charge carrier concentration required for high proton conductivity.

One approach now followed at 3M is to modify the PFSA side chains such that they carry more than one acid site. Such multi-acid side chain ionomer membranes have the potential to demonstrate the mechanical properties of a higher EW polymer (characteristic of a single acid site per side chain), and the proton conduction properties of a lower EW material (conferred by the presence of multi-acid sites per side chain). In this way, a low EW material is created from a high EW polymer. The water soluble fraction, dimensional swelling in water, and the hydration number of 3M™ multi-acid side-chain membranes are all lower than those of PFSA membranes of corresponding low EWs.[14]

Other strategies for limiting membrane swelling are being developed. In general, chemical crosslinking is an effective method of improving polymer mechanical properties, and a series of approaches for the covalent crosslinking of PFSAs, either through the sulfonic acid side chain or through the main chain, have been screened. Several researchers have developed LSC ionomers having sulfonamide functionalities that are reacted to form sulfonimide crosslinks.[15,16] Also, new perfluoropolymers with crosslinkable side chains have been developed by copolymerization of novel multifunctional monomers. For example, substituted TFE monomer units have been designed with pendant perfluoronitrile,[17] perfluorobutyl, and perfluorosulfonamide groups that lead respectively to triazine, perfluorobutyl, or sulfonimide crosslinks after copolymerization. In a different approach Solvay applied the insertion during polymerization of partially fluorinated bi-functional monomeric units derived from tetrafluoroethylene, fluorinated monomeric units containing sulfonyl groups $-SO_2F$, and from 0.01% to 5% by moles of monomeric units deriving from a bis-olefin of formula $R_1R_2C=CH-(CF_2)_m-CH=CR_5R_6$ (where m=2–10, R_1, R_2, R_5, R_6, equal to or different from each other, are H or C_1-C_5 alkyl groups).[18] The membranes are obtained by crosslinking the sulfonic fluorinated polymer and the backbone of the polymer. The consequences of crosslinking during polymerization are an increase in the average molecular weight proportional to the crosslinking agent used and a broadening of the molecular weight distribution. These types of approaches covalently crosslink the hydrophobic regions of ionomer chains and, to some extent, allow the sulfonic acid functions to self-organize into hydrophilic domains. Also, the ion exchange sites are

not consumed during the crosslinking reaction. Characterization of the degree of crosslinking in such systems is not a trivial problem. In the case of sulfonimide crosslinked membranes, X-ray photoelectron spectroscopy in the nitrogen and sulfur binding energy regions has been proven to be useful and has provided an analytical handle enabling the optimization of crosslinking conditions and semi-quantitative determination of the degree of crosslinking.[16]

Better Membranes Through Composite Approaches

Various approaches to producing macrocomposite dimensionally stabilized PFSA membranes have been developed.[19] In the most well-established approach, the ionomer is embedded into expanded poly(tetrafluoroethylene) (PTFE) to produce Gore-Select-type membranes.[20] The improvement in mechanical properties and dimensional stability of these membranes allows preparation of very thin (down to ca. 5 μm) membranes with low area resistance. Other types of porous reinforcing supports are currently emerging. In particular, microporous nanofiber mats can be produced by electrospinning. These non-woven materials possess a high volume fraction of void space and a large surface area to provide high pore interconnectivity and an extensive interface between the two phases. This, along with their nonwoven structure, leads to reinforcement throughout the entire thickness of the membrane. In the literature,[21] two different fabrication approaches have been pursued. One consists of embedding an ionomer into a non- or less-conductive nanofiber mat, while the other involves the incorporation of PFSA nanofibers into an inert matrix. In both cases, the properties of proton conduction and mechanical strength are dissociated between the electrospun reinforcement and the matrix polymer. Electrospun nanofibers of chemically stable and mechanically strong polymers like polyvinylidene fluoride, poly(phenyl sulfone), polybenzimidazole (PBI), and polyimide show exceptional tensile strength and stiffness particularly because of the orientation phenomena resulting from extensional forces experienced by the macromolecular chains during the process.

For example, on embedding low EW Aquivion® into non-welded electrospun PBI nanofiber mats, the ionic crosslinking between the basic sites of PBI and the acidic sites of the ionomer provides an additional reinforcing effect to bind the nanofiber mat and the ionomer three-dimensionally, even across the membrane thickness. PBI-reinforced crosslinked (branched, high molecular weight) 700 EW Aquivion® has shown exceptional durability on OCV hold combined with wet/dry cycling between dry and supersaturated feed gases (an AST designed to accelerate both chemical and mechanical degradation processes) and outstanding stability during an extended accelerated aging regime. In fact, in a test protocol involving more than 2,300 h of operation at 80 °C and 30% RH, which included load cycling, stop/start cycling, and continuous operation, the OCV decreased from 0.98 to 0.93 V only, and the voltage decay was only 3% at 300 mA cm^{-2}. In this case, the mechanical reinforcement properties are probably supplemented by the chemical degradation mitigation effect of PBI. Inorganic fibers of ZrP/ZrO$_2$ obtained by reactive coaxial electrospinning have also been used to form nanocomposite systems with 700 EW SSC Aquivion®.[22] Such nanofibers induced an increase of membrane stiffness with respect to both cast and extruded Aquivion®, including under high temperature and high humidity conditions. More generally, PFSA membranes can be very effectively strengthened by the presence of a nanometric inorganic component, particularly when there is an interaction through hydrogen bonding or proton transfer between the sulfonic acid sites of PFSA and the inorganic material.[19] This interfacial interaction leads to an increase in the modulus and reduced membrane swelling.

The conductivity of single nanofibers of Nafion® is reported to be an order of magnitude higher than that of Nafion®, and this is ascribed to orientation of ionic domains along the Nafion® nanofiber axis.[23] PFSA cannot be electrospun directly due to insufficient interchain entanglement. However, use of a carrier polymer such as a high molecular weight polyethylene oxide (PEO) allows PFSA nanofibers to be electrospun to a very high volume fraction, as shown in **Figure 7** for Aquivion®.[24] The amount of carrier polymer can be further reduced through the use of short-side-chain, low EW PFSAs which gives greater viscosity due to the greater ionic interactions.[24] Composite membranes utilizing inert polymers embedded into ionomer fibers have been fabricated by electrospinning Nafion® and 3M™ PFSA with improved mechanical properties. Composite membranes have also been fabricated by dual-fiber electrospinning[25] using Nafion® for PEMFC or functionalized polysulfone for alkaline fuel cells.

The amount of carrier polymer can be further reduced through the use of short-side chain and low EW PFSAs which give greater viscosity due to the greater ionic interactions (**Table 1**).

Table 1. Concentrations of Aquivion® and PEO, PEO molecular weight, and solvents used in electrospinning Aquivion® nanofibers of various equivalent weights.

EW	Solvent	Applied Voltage (kV)	PEO Mol. Wt.	PFSA Concentration	PEO Concentration
700	DMF/H$_2$O	15	2×10^6	15%	0.3%
830	DMAc/H$_2$O	15	2×10^6	18%	0.4%
950	1-Propanol/DMAc/H$_2$O	13	2×10^6	13 %	0.2 %
980	DMAc/EtOH	13	1×10^6	18%	1%
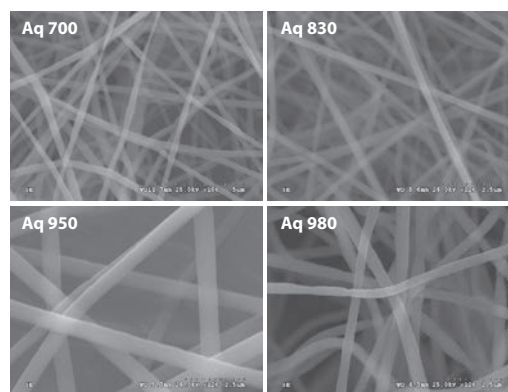
Figure 7. Scanning electron micrographs of Aquivion® electrospun nanofibers of EW 700, 830, 950, and 980.

Catalyst Ink and Fuel Cell Operation

The ionomer is an essential component of catalyst inks, since it extends the reaction zone and increases electrocatalyst utilization. To date, little is published on the use of the SSC ionomer in catalyst inks for coating fuel cell membranes or gas diffusion media. However, improved cell performance has been observed in MEAs comprising the SSC ionomer compared to baseline MEAs incorporating the LSC ionomer, particularly when the cell is operated at high temperature (90–140 °C) and low RH (dry-20%).[26] This suggests the low EW SSC ionomers favor water mobility, proton conductivity, and oxygen reduction reaction kinetics through self-humidification during low RH operation. Furthermore, increased Pt utilization and effectiveness have been obtained. This may be considered indicative of increased accessibility of SSC ionomers to the graphitized carbon surface and Pt nanoparticles arising from more uniform and continuous coverage of catalyst and carbon particles.[27] Polarization curves

obtained with Nafion®-111 and Aquivion® E79-03S membranes under a pressure of 1.5 bar absolute and at temperatures 80–110 °C show that the SSC membrane is better able to sustain high temperature operation (**Figure 8**).[28] The lower RH conditions at the cathode rather than the anode during this testing also provides insight into the ability of each type of membrane electrode assembly to utilize the water produced at the cathode. Thus differences in performance result from differences in the ohmic resistance which, in turn, is related to effective proton mobility and the rate of water flux through the membrane. Studies indicate that increasing the membrane IEC beyond an optimal value does not necessarily provide increased water transport and effective proton mobility due to the inherent link between water permeation and proton mobility.[29] Furthermore, comparative load cycling at 120 °C and 40% RH led to a greater increase in membrane resistance with Nafion®-based MEAs than with Aquivion®-based MEAs.[30] Finally, while LSC Nafion® has for many years been essentially the only electrolyte used in proton exchange membrane water electrolysers, recent studies using SSC Aquivion® allow electrolyser operation up to 140 °C,[31] low hydrogen crossover (<1 mA/cm^2 at 1 bar absolute pressure), and high performance (1,650 mV at 2 A/cm^2).
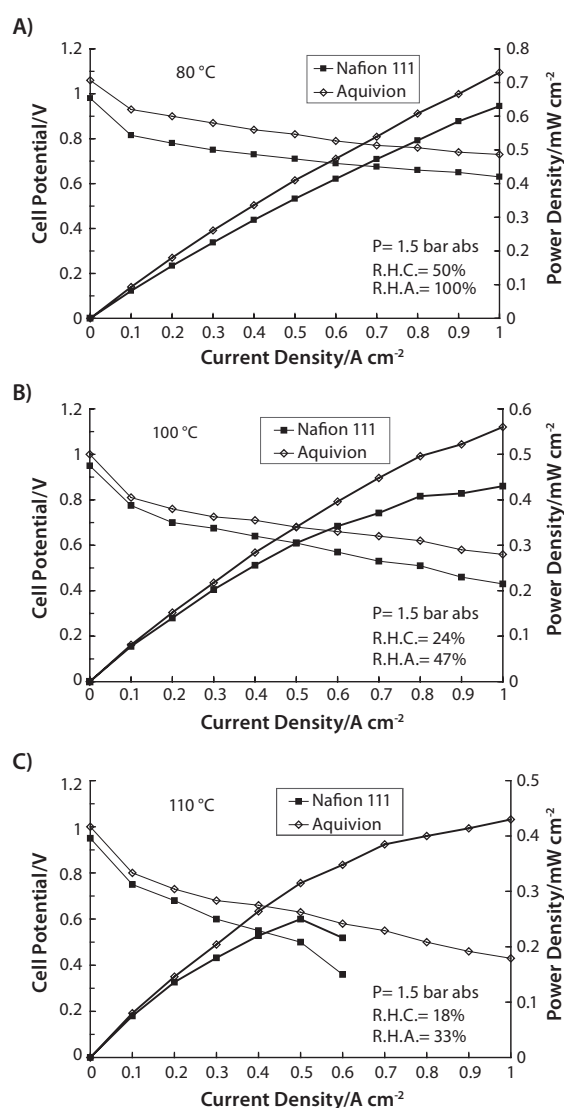
Summary

Comparison of the compositional and structural differences of various PFSA membranes reveals materials that possess short side chains (SSC) possess higher crystallinity and heat of fusion. Also, the presence of SSC leads to higher water uptake and enhanced proton conductivity and provides higher tolerance toward the free radical attack leading to increased durability of the membranes. Thus, the presence of SSC in Aquivion® membranes makes them attractive for high temperature, high performance proton exchange membrane fuel cells, and proton exchange membrane water electrolysers.

References

(1) Hickner, M. A.; Ghassemi, H.; Kim, Y. S.; Einsla, B. R.; McGrath, J. E. *Chem. Rev.* **2004**, *104*, 4587–4611.
(2) Ezzell, B. R.; Carl, W. P.; Mod, W. A.; The Dow Chemical Company: US 4,358,412, **1980**.
(3) Arcella, V.; Ghielmi, A.; Tommasi, G. *Ann. New York Acad. Sci.* **2003**, *984*, 226–244.
(4) Emery, M.; Frey, M.; Guerra, M.; Haugen, G.; Hintzer, K.; Lochhaas, K. H.; Pham, P.; Pierpont, D.; Schaberg, M.; Thaler, A.; Yandrasits, M. A.; Hamrock, S. J. *ECS Trans.* **2007**, *11*, 3–14.
(5) Curtin, D. E.; Lousenberg, R. D.; Henry, T. J.; Tangeman, P. C.; Tisack, M. E. *J. Power Sources* **2004**, *131*, 41–48.
(6) Ghielmi, A.; Vaccarono, P.; Troglia, C.; Arcella, V. *J. Power Sources* **2006**, *145*, 108–115.
(7) Liu, Y.; Horan, J. L.; Schlichting, G. J.; Caire, B. R.; Liberatore, M. W.; Hamrock, S. J.; Haugen, G. M.; Yandrasits, M. A.; Seifert, S.; Herring, A. M. *Macromolecules* **2012**, *45*, 7495–7503.
(8) Mauritz, K. A.; Moore, R. B. *Chem. Rev.* **2004**, *104*, 4535–4585.
(9) Gebert, M.; Merlo, L.; Arcella, V. *ECS Trans.* **2011**, *30*, 91–95.
(10) Merlo, L.; Ghielmi, A.; Cirillo, L.; Gebert, M.; Arcella, V. *J. Power Sources* **2007**, *171*, 140–147.
(11) Ghassemzadeh, L.; Kreuer, K. D.; Maier, J.; Müller, K. J. *Power Sources* **2011**, *196*, 2490–2497.
(12) Danilczuk, M.; Perkowski, A. J.; Schlick, S. *Macromolecules* **2010**, *43*, 3352–3358.
(13) Zaton, M.; Jones, D. J.; Rozière, J. manuscript in preparation **2015**.
(14) Schaberg, M. S.; Abulu, J. E.; Haugen, G. M.; Emery, M. A.; O'Conner, S. J.; Xiong, P. N.; Hamrock, S. J. *ECS Trans.* **2010**, *33*, 627–633.
(15) Uematsu, N.; Hoshi, N.; Koga, T.; Ikeda, M. *J. Fluorine Chem.* **2006**, *127*, 1087–1095.
(16) Zhang, Y.; Li, L.; Tang, J. K.; Bauer, B.; Zhang, W.; Gao, H. R.; Taillades-Jacquin, M.; Jones, D. J.; Rozière, J.; Lebedeva, N.; Mallant, R. K. A. M. *ECS Trans.* **2009**, *25*, 1469–1472.
(17) Yandrasits, M. A.; Hamrock, S. J.; Grootaert, S. J.; 3M Innovative Properties Company: US 20,050,107,489 A1, **2005**.
(18) Ghielmi, A.; Arcella, V.; Solvay Solexis EP1238999 B1, **2006**.
(19) Subianto, S.; Pica, M.; Casciola, M.; Cojocaru, P.; Merlo, L.; Jones, D. J.; Hards, G. *J. Power Sources* **2013**, *233*, 216–230.
(20) Penner, R. M.; Martin, C. R. *J. Electrochem. Soc* **1985**, *132*, 514.
(21) Subianto, S.; Giancola, S.; Ercolano, G.; Nabil, Y.; Jones, D. J.; Rozière, J.; Cavaliere, S. *Electrospinning for Advanced Energy and Environmental Applications*; Cavaliere, S., Ed.; CRC Press **2015**, 29–60.
(22) Subianto, S.; Donnadio, A.; Cavaliere, S.; Pica, M.; Casciola, M.; Jones, D. J.; Rozière, J. *J. Mater. Chem. (A)* **2014**, *2*, 13359–13365.
(23) Dong, B.; Gwee, L.; Salas-de la Cruz, D.; Winey, K. I.; Elabd, Y. A. *Nano Lett.* **2010**, *10*, 3785–3790.
(24) Subianto, S.; Cavaliere, S.; Jones, D. J.; Rozière, J. *J. Polym. Sci. Part A: Polym. Chem.* **2013**, *51*, 118–128.
(25) Ballengee, J. B.; Pintauro, P. N. *J. Membr. Sci.* **2013**, 442, 187–195.
(26) Peron, J.; Edwards, D.; Haldane, M.; Luo, X.; Zhang, Y.; Holdcroft, S.; Shi, Z. *J. Power Sources* **2011**, *196*, 179–181.
(27) Park, Y.-C.; Kakinuma, K.; Uchida, H.; Watanabe, M. *J. Power Sources* **2015**, *275*, 384–391.
(28) Aricò, A. S.; Di Blasi, A.; Brunaccini, G.; Sergi, F.; Dispenza, G.; Andaloro, L.; Ferraro, M.; Antonucci, V.; Asher, P.; Buche, S.; Fongalland, D.; Hards, G. A.; Sharman, J. D. B.; Bayer, A.; Heinz, G.; Zandonà, N.; Zuber, R.; Gebert, M.; Corasaniti, M.; Ghielmi, A.; Jones, D. J. *Fuel Cells* **2010**, *10*, 1013–1023.
(29) Zhao, N.; Edwards, D.; Lai, C.; Wang, K.; Li, J.; Zhang, Y.; Holdcroft, S.; Shi, Z. *J. Power Sources* **2013**, *242*, 877–883.
(30) Jeon, Y.; Na, H.; H. Hwang; J. Park; H. Hwang; Shul, Y. *Int. J. Hydrogen Energy* **2015**, *40*, 3057–3067.
(31) Skulimowska, A.; Zaton, M.; Dupont, M.; Sunde, S.; Merlo, L.; Jones, D. J.; Rozière, J. *Int. J. Hydrogen Energy* **2014**, *39*, 6307–6316.
(32) Arcella, V.; Troglia, C.; Ghielmi, A. *Ind. Eng. Chem. Res.* **2005**, *44*, 7646–7651.
(33) Tant, M. R.; Darst, K. P.; Lee, K. D.; Martin, C. W. *ACS Symp. Ser.* **1989**, *395*, 370–400.

Figure 8. Polarization curves obtained with Nafion®-111 and Aquivion®-based MEAs under 1.5 bar abs. at 80–110 °C, at indicated relative humidities at the anode (RHA) and cathode (RHC). Reproduced from Reference 28. Copyright 2010 Wiley-VCH.

Aquivion® Membrane Sheets

For a complete list of available materials, visit aldrich.com/membranes.

Product Name	Description	Dimension (L × W × thickness)	Prod. No.
Aquivion® E87-05S	PFSA eq. wt. 870 g/mole SO₃H	18 cm × 18 cm × 50 μm	802719-1EA
Aquivion® E87-05S		31 cm × 31 cm × 50 μm	802727-1EA
Aquivion® E87-12S		18 cm × 18 cm × 120 μm	802786-1EA
Aquivion® E87-12S		31 cm × 31 cm × 120 μm	802514-1EA
Aquivion® E98-05	PFSA eq. wt. 980 g/mole SO₃H	31 cm × 31 cm × 50 μm	802697-1EA
Aquivion® E98-05		18 cm × 18 cm × 50 μm	802670-1EA
Aquivion® E98-05S		31 cm × 31 cm × 50 μm	802700-1EA
Aquivion® E98-05S		18 cm × 18 cm × 50 μm	802689-1EA
Aquivion® E98-09S		18 cm × 18 cm × 90 μm	802735-1EA
Aquivion® E98-09S		31 cm × 31 cm × 90 μm	802743-1EA
Aquivion® E98-15S		18 cm × 18 cm × 150 μm	802751-1EA
Aquivion® E98-15S		31 cm × 31 cm × 150 μm	802778-1EA

Aquivion® Membrane Materials

For a complete list of available materials, visit aldrich.com/membranes.

Product Name	Description	Form	Prod. No.
Aquivion® D72-25BS	PFSA eq. wt. 700 g/mole SO₃H	dispersion liquid	802549-25ML
Aquivion® D79-25BS	PFSA eq. wt. 790 g/mole SO₃H	dispersion liquid	802565-25ML
Aquivion® D79-25BS-Li	PFSA eq. wt. 980 g/mole SO₃Li	dispersion liquid	802573-25ML
Aquivion® D83-06A	PFSA wq. wt. 830 g/mole SO₃H	dispersion liquid	802603-50ML
Aquivion® D83-24B	PFSA eq. wt. 830 g/mole SO₃H stabilized CF₃ polymer chain ends	dispersion liquid	802654-25ML
Aquivion® D98-25BS	PFSA eq. wt. 980 g/mole SO₃H	dispersion liquid	802557-25ML
Aquivion® P87S-SO₂F	PFSA eq. wt. 870 g/mole SO₂F	cylinder (pellet)	802530-50G
Aquivion® P98-SO₂F	PFSA eq. wt. 870 g/mole SO₂F	cylinder (pellet)	802662-50G
Aquivion® PW79S	PFSA eq. wt. 790 g/mole SO₃H	coarse powder	802611-25G
Aquivion® PW79S-Li	PFSA eq. wt. 790 g/mole SO₃Li	coarse powder	802581-10G
Aquivion® PW87S	PFSA eq. wt. 870 g/mole SO₃H	coarse powder	802646-25G
Aquivion® PW98	PFSA eq. wt. 980 g/mole SO₃H	coarse powder	802638-25G

Nafion® Membrane Sheets

For a complete list of available materials, visit aldrich.com/membranes.

Product Name	Size	Equivalent Weight	Mfg. Number	Prod. No.
Nafion® perfluorinated membrane	L × W 12 × 12 in. thickness 0.005 in.	1,100	Nafion® 115	541346-1EA
Nafion® perfluorinated membrane	thickness 0.007 in. L × W 8 × 10 in.	1,100	Nafion® 117	274674-1EA
Nafion® perfluorinated membrane	thickness 0.007 in. L × W 12 × 12 in.	1,100	Nafion® 117	292567-1EA
Nafion® perfluorinated membrane	L × W 12 × 12 in. thickness 0.006 in.	-	Nafion® 324	565067-1EA
Nafion® perfluorinated membrane	thickness 0.013 in. L × W 12 × 12 in.	1,100	Nafion® 424	563994-1EA
Nafion® perfluorinated membrane	thickness 0.002 in. L × W 12 × 12 in.	1,100	Nafion® NRE-212	676470-1EA

Membrane Materials

For a complete list of available materials, visit **aldrich.com/membranes**.

Product Name	Form	Equivalent Weight	Prod. No.
Disodium bis(4-chloro-3-sulfophenyl)sulfone	-	-	730882-5G
Nafion® 117 solution	~ 5% in a mixture of lower aliphatic alcohols and water	-	70160-25ML 70160-100ML
Nafion® NR50	pellets	≤1250	309389-10G 309389-25G
Nafion® perfluorinated resin solution	5 wt. % in mixture of lower aliphatic alcohols and water	1,100	510211-25ML 510211-100ML
Nafion® perfluorinated resin solution	5 wt. % in lower aliphatic alcohols and water	1,100	274704-25ML 274704-100ML 274704-500ML
Nafion® perfluorinated resin solution	20 wt. % in lower aliphatic alcohols and water	-	663492-25ML 663492-100ML
Nafion® perfluorinated resin solution	20 wt. % in mixture of lower aliphatic alcohols and water	1,100	527122-25ML 527122-100ML
Nafion® perfluorinated resin solution	5 wt. % in mixture of lower aliphatic alcohols and water	1,000	527084-25ML
Nafion® perfluorinated resin, aqueous dispersion	10 wt. % in H_2O	1,000	527114-25ML
Nafion® perfluorinated resin, aqueous dispersion	10 wt. % in H_2O	1,100	527106-25ML
Nafion® perfluorinated resin, powder	powder	1,100	495786-500MG
Nafion®, trimethylsilylated	-	-	392928-10G 392928-25G
Polystyrene-*block*-poly(ethylene-*ran*-butylene)-*block*-polystyrene, sulfonated solution	5 wt. % in 1-propanol and dichloroethane	-	448885-25ML 448885-100ML
Poly(vinylphosphonic acid)	powder	-	661740-1G
Poly(2-vinylpyridine-*co*-styrene)	granular	-	184608-50G

OLIVINE-TYPE CATHODE MATERIALS
FOR LITHIUM-ION BATTERIES

Izumi Taniguchi
Department of Chemical Engineering
Graduate School of Science and Engineering, Tokyo Institute of Technology
12-1, Ookayama-2, Meguro-ku, Tokyo 152-8552, Japan
Email: taniguchi.i.aa@m.titech.ac.jp

Introduction

Lithium-ion batteries (LIBs) have been widely adopted as the most promising portable energy source in electronic devices because of their high working voltage, high energy density, and good cyclic performance. Currently, LIBs are used in electric vehicles and hybrid electric vehicles as well. In these batteries, olivine-type cathode materials such as $LiMPO_4$ (M=Fe and Mn) have attracted significant interest, especially due to their low cost and high intrinsic safety. However, they show poor electrochemical properties mainly due to their low electrical conductivities. Thus far, a number of attempts have been made to enhance the electrochemical properties of olivine-type cathode materials, including particle-size reduction,[1] cation doping,[2] carbon coating of $LiMnPO_4$,[3] and use of $LiMnPO_4$/carbon composite.[2,4] Several synthesis routes have been developed to overcome the weakness of $LiMnPO_4$[3] such as solid-state reaction,[4–6] sol-gel method,[2,3] polyol process,[7] hydrothermal synthesis[8] precipitation,[9] and electrostatic spray deposition.[10] However, the electrochemical performance of $LiMPO_4$ cathodes prepared using the aforementioned techniques does not yet meet the application needs of commercial cells.

Spray pyrolysis (SP) is a well-known continuous and single-step method for the preparation of fine homogeneous high-purity multicomponent powders. Compared to particles prepared by soft chemistry methods, SP yields a narrow particle size distribution that can be controlled from the micrometer to sub-micrometer scale. Moreover, SP can be used to achieve highly pure powders with easily controllable composition. About a decade ago we first reported that the spherical nanostructured $LiMn_2O_4$ and its substituted forms could be prepared by spray pyrolysis.[11,12] Recently, we have also reported that $LiMPO_4$/C (M=Fe, Mn, Co) nanocomposites[13–16] with excellent electrochemical properties can be successfully synthesized using a combination of SP, ball milling, and heat treatment. Some of our recent results on $LiMPO_4$/C composites are summarized in this article.

Synthesis and Electrochemical Properties of $LiFePO_4$/C Nanocomposites

$LiFePO_4$/C nanocomposites were prepared at 500 °C by SP and then wet-ball milled (WBM) at a rotating speed of 800 rpm. The WBM with ethanol was performed for 3 h in an Ar atmosphere, and the milled mixture was heat-treated at 600 °C for 4 h in a N_2+3% H_2 atmosphere. Transmission electron microscopy (TEM) revealed that the $LiFePO_4$ nanoparticles, with a geometric mean diameter of 146 nm, were coated with a thin carbon layer of several nanometers (**Figure 1**).
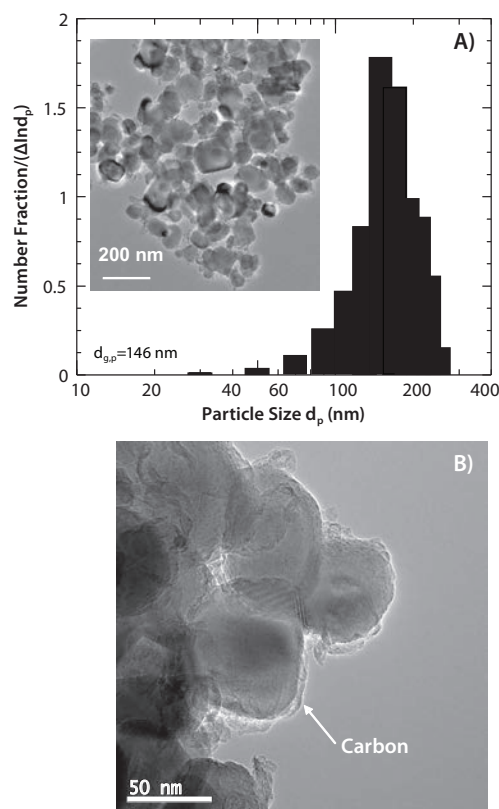
Figure 1. TEM images and particle size distribution of the sample prepared by the combination of spray pyrolysis and wet-ball milling followed by heat treatment.

The first charge-discharge profiles of cells containing carbon-coated $LiFePO_4$ nanoparticles with increasing charge-discharge rate from 0.1 to 60 C between 2.5 and 4.3 V are presented in **Figure 2**. At a charge-discharge rate of 0.1 C, the cell has a discharge capacity of 165 mAh g^{-1}, which corresponds to 96% of the theoretical

capacity of LiFePO$_4$ (170 mAh g^{-1}) and a much smaller polarization loss and irreversible capacity. A wide flat voltage plateau corresponding to the Fe^{+2}/Fe^{+3} redox reaction is observed at 3.4 V. The first discharge capacities at charge-discharge rates of 1, 5, 10, and 20 C are 155, 130, 118, and 105 mAhg^{-1}, respectively. Even at a rate of 60 C, the electrode containing carbon-coated LiFePO$_4$ nanoparticles has a discharge capacity of 75 mAh g^{-1}.
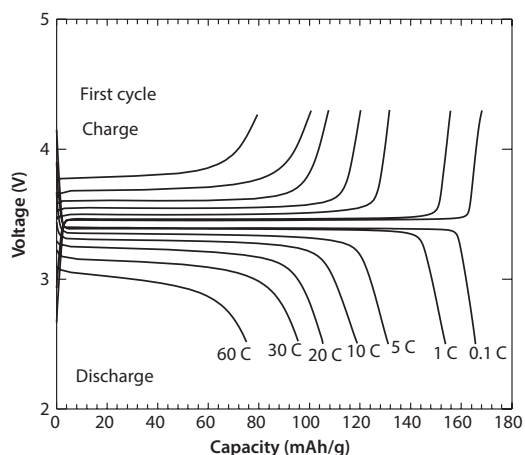
Figure 2. Charge-discharge curves at 1st cycle of carbon-coated LiFePO$_4$ nanoparticles.

The cyclic performance of the cells containing carbon-coated LiFePO$_4$ nanoparticles at different charge-discharge rates was investigated over 100 cycles, and the results are given in **Figure 3**. The cells exhibit an excellent cyclic property. The cells show no capacity fading even after 100 cycles at different charge-discharge rates ranging from 1 to 60 C. These results demonstrate that the structure of the carbon-coated LiFePO$_4$ nanoparticles is very stable, and the electrochemical lithium-ion insertion/extraction process is quite reversible even at high charge-discharge rates. These results indicate that the preparation approach using the combination of SP and WBE followed by heat treatment enables to achieve a high rate performance for LiFePO$_4$ composite electrode materials.
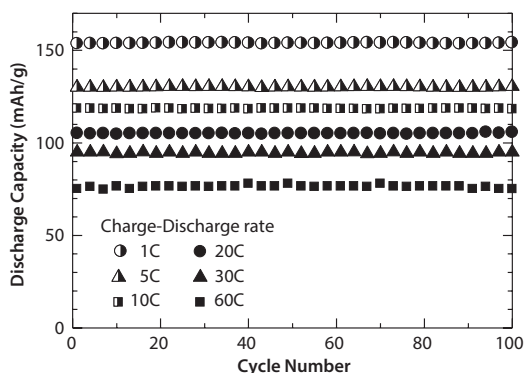
Figure 3. Cycle performance of carbon-coated LiFePO4 nanoparticles.

Synthesis and Electrochemical Properties of LiMnPO$_4$/C Nanocomposites

LiMnPO$_4$/C nanocomposites were prepared using a combination of SP, WBM and heat treatment. The SP was performed at 300 °C, whereas the heat treatment was performed at 500 °C for 4 h in a N$_2$+3% H$_2$ atmosphere. X-ray diffraction (XRD) was used to confirm the ordered

LiMnPO$_4$ olivine structure without any impurity phases. The scanning electron microscopy (SEM) and TEM also confirmed that the final sample was the LiMnPO$_4$/C nanocomposite with a primary particle size of 100 nm. The TEM of the final sample is shown in **Figure 4**. Both phases of carbon and LiMnPO$_4$ could be seen in this image.
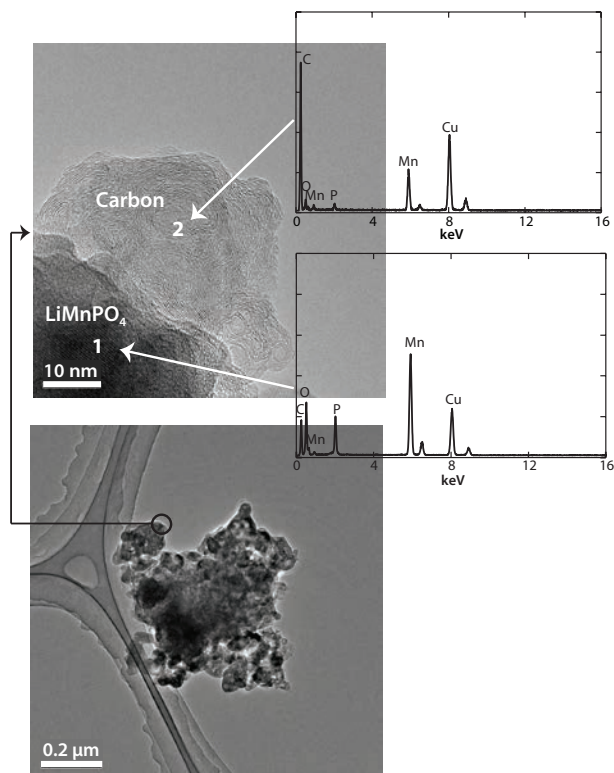
Figure 4. TEM images of the LiMnPO$_4$/C nanocomposite prepared by a combination of SP (at 300 °C) and WBM followed by heat treatment at 500 °C.

Figure 5 shows the initial charge-discharge profiles of the cells evaluated at constant current (CC)-constant voltage (CV) charge mode up to the cutoff voltage of 4.4 V and then CC discharge at various rates. The flat discharge plateau could still be recognized even at discharge rate of 2 C. This is attributed to the deep Li extraction level under very low currents in CV charge stage.
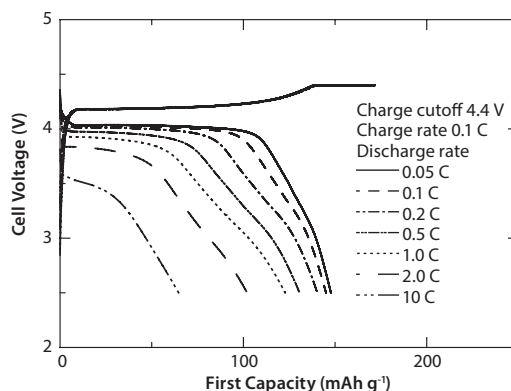
Figure 5. First charge/discharge curves at CC-CV charge condition of the cells containing the LiMnPO$_4$/C nanocomposites prepared by the combination of SP (at 300 °C) and WBM followed by heat treatment at 500 °C.

Figure 6 shows the rate capabilities determined for three charging modes: (1) CC charge up to 4.4 V, (2) CC charge up to 4.8 V, and (3) CC charge up to 4.4 V followed by CV charge reaching to theoretical capacity for

LiMnPO$_4$/C nanocomposite containing cell. At the discharge rate of 0.05 C, the cell exhibits the first discharge capacity of 123, 153, and 147 mAh g^{-1} in CC-4.4 V, CC-4.8 V and CC-CV modes, respectively. At a discharge rate of 1 C, the initial discharge capacity of 51, 107, and 123 mAh g^{-1} were observed for CC-4.4 V, CC-4.8 V and CC-CV modes, respectively. Even with a discharge rate of 10 C, the cell could deliver capacity of 65 mAh g^{-1} in CC-CV mode. In spite of the intrinsic low electronic and ionic conductivities of LiMnPO$_4$, the cells containing LiMnPO$_4$/C nanocomposites exhibit very good rate capability, which could be attributed to the large specific surface area, the small primary particle size, and a uniform carbon distribution.
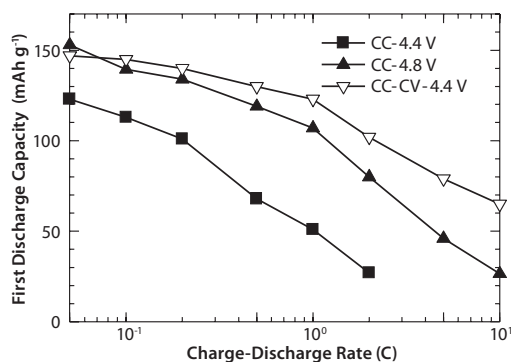
Figure 6. Rate capability of the cells containing the LiMnPO$_4$/C nanocomposites prepared by the combination of SP (at 300 °C) and WBM followed by heat treatment.

The cycle performance comparison between three charge modes is shown in **Figure 7**. The cells containing LiMnPO$_4$/C nanocomposites show good cycle performance for all the three different charging modes.
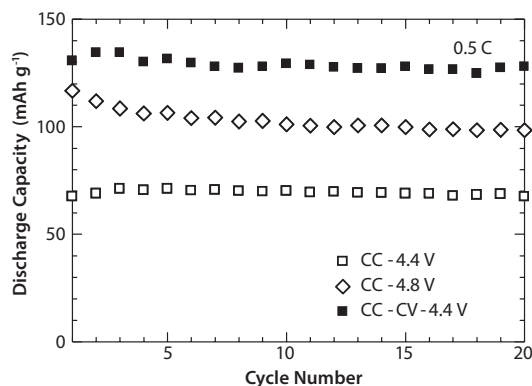
Figure 7. Cycle performance at different charge modes of the cells containing the LiMnPO$_4$/C nanocomposites prepared by the combination of SP at 300 °C and WBM followed by heat treatment.

Synthesis and Electrochemical Properties of LiCoPO$_4$/C Nanocomposites

LiCoPO$_4$/C nanocomposite also was successfully prepared by using a combination of SP and WBM followed by heat treatment. The SP was performed at 300 °C, whereas the heat treatment was performed at 500 °C for 4 h in a N$_2$+3% H$_2$ atmosphere. The XRD analysis confirms that the LiCoPO$_4$/C nanocomposite is well crystallized in an orthorhombic structure with *Pmna* space group. SEM and TEM equipped with energy dispersive spectroscopy technique reveals that the LiCoPO$_4$/C nanocomposites are agglomerates of LiCoPO$_4$ primary particles with a geometric mean diameter of 87 nm, and the carbon is well distributed on the surface of the agglomerates.

Figure 8 presents the first discharge profile of the cells containing LiCoPO$_4$/C nanocomposites as active cathode materials at 0.1 C. For comparison, the discharge profile of cells containing LiCoPO$_4$ is also shown in the same figure. The LiCoPO$_4$/C nanocomposite cathode exhibits a wide and flat voltage plateau around 4.75 V. It can be noted that in comparison to LiCoPO$_4$, the LiCoPO$_4$/C nanocomposite cathode delivers a larger discharge capacity (94 mAh g^{-1} for LiCoPO$_4$ vs. 141 g^{-1} LiCoPO$_4$/C nanocomposite). **Figure 9** shows the rate capabilities of the cells containing LiCoPO$_4$ and LiCoPO$_4$/C nanocomposites. The cells containing LiCoPO$_4$ exhibit first discharge capacities of 99, 94, 78, 53, and 11 mAh g^{-1} at 0.05, 0.1, 1, 5, and 20 C, respectively; the cell containing LiCoPO$_4$/C nanocomposites shows first discharge capacities of 142, 141, 137, 128, and 109 mAh g^{-1} at 0.05. 0.1, 1, 5, and 20 C, respectively.
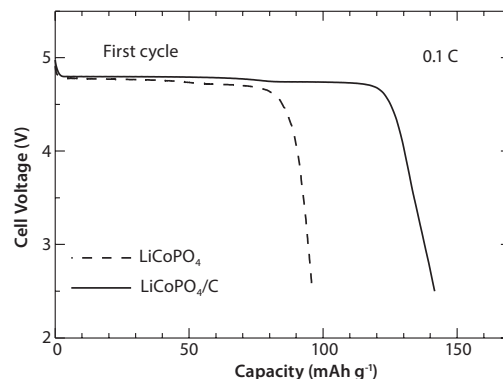
Figure 8. First discharge profiles of the cells containing LiCoPO$_4$/C nanocomposite cathode at 0.1 C.
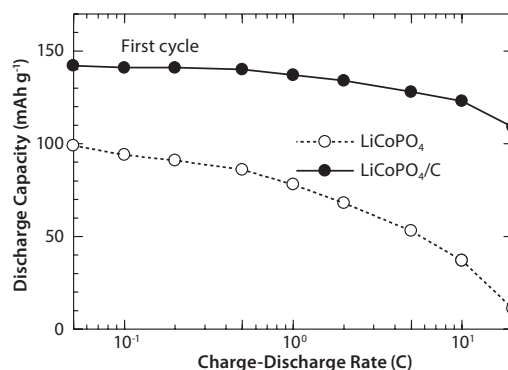
Figure 9. Rate capabilities of the cells containing LiCoPO$_4$/C nanocomposite cathode.

Conclusion

To summarize, the Li*M*PO$_4$/C (*M*=Fe, Mn, Co) nanocomposites were successfully synthesized using a combination of spray pyrolysis, ball milling, and heat treatment. The Li*M*PO$_4$/C nanocomposites synthesized using this approach show excellent electrochemical properties with the specific capacities close to that of theoretical values. The results indicate that the combination of spray pyrolysis and ball milling aerosol has the potential to be an effective synthesis route for improving the electrochemical properties of olivine-type cathode materials for lithium-ion batteries.

References

(1) Delacourt, C.; Poizot, P.; Morcrette, M.; Tarascon, J.-M.; Masquelier, C. *Chem. Matter.* **2004**, *16*, 93–99.
(2) Dominko, R.; Bele, M.; Gaberscek, M.; Remskar, M.; Hanzel, D.; Goupil, J. M.; Pejovnik, S.; Jamnik, J. *J. Power Sources.* **2006**, *153*, 274–280.
(3) Yang, J.; Xu, J. J. *J. Electrochem. Soc.* **2006**, *153*, A716–A723.
(4) Bramnik, N. N.; Ehrenberg, H. *J. Alloy. Comp.* **2008**, *464*, 259–264.
(5) Yonemura, M.; Yamada, A.; Takei, Y.; Sonoyama, N.; Kanno, R. *J. Electrochem. Soc.* **2004**, *151*, A1352–A1356.
(6) Padhi, A. K.; Nanjundaswamy, K. S.; Goodenough, J. B. *J. Electrochem. Soc.* **1997**, *144*, 1188–1194.
(7) Wang, D.; Buqa, H.; Crouzet, M.; Deghenghi, G.; Drezen, T.; Exnar, I.; Kwon, N.-H.; Miners, J. H.; Poletto, L.; Grätzel, M. *J. Power Sources.* **2009**, *189*, 624–628.

(8) Fang, H.; Pan, Z.; Li, L.; Yang, Y.; Yan, G.; Li, G.; Wei, S. *Electrochem. Commun.* **2008**, *10*, 1071–1073.
(9) Delacourt, C.; Laffont, L.; Bouchet, R.; Wurm, C.; Leriche, J.-B.; Morcrette, M.; Tarascon, J.-M.; Masquelier, C. *J. Electrochem. Soc.* **2005**, *152*, A913–A921.
(10) Ma, J.; Qin, Q.-Z. *J. Power Sources.* **2005**, *148*, 66–71.
(11) Bakenov, Z.; Taniguchi, I. *Solid State Ionics.* **2005**, *176*, 1027–1034.
(12) Taniguchi, I. *Mater. Chem. Phys.* **2005**, *92*, 172–179.
(13) Konarova, M.; Taniguchi, I. *J. Power Sources.* **2009**, *194*, 1029–1035.
(14) Konarova, M.; Taniguchi, I. *J. Power Sources.* **2010**, *195*, 3661–3667.
(15) Doan, T. N. L.; Taniguchi, I. *J. Power Sources.* **2011**, *196*, 1399–1408.
(16) Doan, T. N. L.; Taniguchi, I. *J. Power Sources.* **2011**, *196*, 5679–5684.

Electrode Sheets

Sheet size 5 × 10 in./80% active material on aluminum electrode substrate.

For a complete list of electrode sheets, visit aldrich.com/lib.

Product Name	Composition	Purity	Nominal Voltage (V)	Capacity (minimum)	Capacity (nominal)	Prod. No.
Lithium manganese nickel oxide, LMNO	$Li_2Mn_3NiO_8$	≥98%	4.7 (Li/Li⁺)	115 mAh/g	125 mAh/g	765198-1EA
Lithium manganese oxide, LMO	$LiMn_2O_4$	≥98%	4.7 (Li/Li⁺)	120 mAh/g	110 mAh/g	765201-1EA
Lithium nickel cobalt aluminium oxide, NCA	$LiNi_{0.8}Co_{0.15}Al_{0.05}O_2$	≥98%	3.7 (Li/Li⁺)	150 mAh/g	180 mAh/g	765171-1EA
Lithium nickel manganese cobalt oxide, NMC	$LiNi_{0.33}Mn_{0.33}Co_{0.33}O_2$	-	3.5 (Li/Li⁺)	210 mAh/g	-	765163-1EA
Lithium titanate, LTO	$Li_4Ti_5O_{12}$	≥98%	1.5 (Li/Li⁺)	150 mAh/g	160 mAh/g	765155-1EA

Cathode Materials

For a complete list of cathode materials, visit aldrich.com/lib.

Product Name	Composition	Description	Dimensions	Prod. No.
Cobalt monoantimonide	CoSb	99.9% trace metals basis	-80 mesh	746320-5G
Lithium cobalt(III) oxide	$LiCoO_2$	powder, 99.8% trace metals basis	-	442704-100G-A
Lithium cobalt phosphate, LCP	$LiCoPO_4$	powder, 99%	-	725145-25G
Lithium cobalt phosphate, LCP	$LiCoPO_4$	powder, 99.9% trace metals basis	-	777110-25G
Lithium iron(III) oxide	$LiFeO_2$	powder, 95%	particle size <1 µm	442712-100G-A
Lithium iron(II) phosphate, LFP	$LiFePO_4$	powder, >97% (XRF)	particle size <5 µm (BET)	759546-5G
Lithium manganese dioxide	$LiMnO_2$	powder, >99% trace metals basis	particle size <1 µm	725137-25G
Lithium manganese nickel oxide, LMNO	$Li_2Mn_3NiO_8$	powder, >99%	particle size <0.5 µm (BET)	725110-25G
Lithium manganese oxide, LMO	$LiMn_2O_4$	powder, >99%	particle size <0.5 µm (BET)	725129-25G
Lithium manganese(III,IV) oxide, LMO	$LiMn_2O_4$	-	particle size <5 µm	482277-25G
Lithium molybdate	Li_2MoO_4	powder or crystals, 99.9% trace metals basis	-	400904-250G
Lithium nickel cobalt aluminium oxide, NCA	$LiNi_{0.8}Co_{0.15}Al_{0.05}O_2$	powder, >98%	particle size <0.5 µm	760994-10G
Lithium nickel cobalt oxide, LNCO	$LiNi_{0.8}Co_{0.2}O_2$	powder, >98%	particle size <0.5 µm	760986-10G
Lithium nickel dioxide, LNO	$LiNiO_2$	powder, ≥98% trace metals basis	particle size <3 µm (BET)	757365-10G
Lithium nickel manganese cobalt oxide, NMC	$LiNi_{0.33}Mn_{0.33}Co_{0.33}O_2$	powder, >98%	particle size <0.5 µm	761001-10G
Manganese nickel carbonate	$Mn_{0.75}Ni_{0.25}CO_3$	powder, 99.99% trace metals basis (excluding Mg)	-	763608-25G

Anode Materials

For a complete list of anode materials, visit aldrich.com/lib.

Product Name	Description	Form	Purity	Prod. No.
Lithium	particle size 4-10 mesh	granular	99%, metals basis	444456-10G 444456-50G
	thickness × W 1.5 × 100 mm	ribbon	99.9% trace metals basis	266000-25G 266000-100G
	thickness × W 0.75 × 45 mm	ribbon	99.9% trace metals basis	265993-25G 265993-100G
	thickness × W 0.75 × 19 mm	ribbon	99.9% trace metals basis	320080-25G 320080-100G
	thickness × W 0.38 × 23 mm	ribbon	99.9% trace metals basis	265985-25G 265985-100G
	diam. 3.2 mm	wire	≥98%	278327-25G 278327-100G

Product Name	Description	Form	Purity	Prod. No.
Lithium-aluminum alloy	-	powder	-	426490-25G
Lithium titanate, LTO	−325 mesh	powder	-	400939-100G
Lithium titanate, spinel, LTO nanopowder	particle size <200 nm (BET)	nanopowder	>99%	702277-25G
Tin(IV) oxide	particle size <100 nm (BET)	nanopowder	-	549657-5G 549657-25G

Electrolyte Solutions

Lithium Hexafluorophosphate Solutions, Battery Grade: H_2O <15 ppm; HF <50 ppm; APHA <50.

For a complete list of electrolyte solutions, visit aldrich.com/lib.

Product Name	Specifications	Prod. No.
1.0 M $LiPF_6$ in EC/DMC=50/50 (v/v)	in ethylene carbonate and dimethyl carbonate	746711-100ML
1.0 M $LiPF_6$ in EC/EMC=50/50 (v/v)	in ethylene carbonate and ethyl methyl carbonate	746738-100ML
1.0 M $LiPF_6$ in EC/DEC=50/50 (v/v)	in ethylene carbonate and diethyl carbonate	746746-100ML
1.0 M $LiPF_6$ in DMC	in dimethyl carbonate	746754-100ML
1.0 M $LiPF_6$ in EMC	in ethyl methyl carbonate	746762-100ML
1.0 M $LiPF_6$ in DEC	in diethyl carbonate	746770-100ML
1.0 M $LiPF_6$ in PC	in propylene carbonate	746789-100ML

Electrolyte Materials

For a complete list of electrolyte materials, visit aldrich.com/lib.

Product Name	Composition	Purity	Prod. No.
Lithium aluminum titanium phosphate	$Li_{1.3}Al_{0.3}Ti_{1.7}(PO_4)_3$	≥99.9% trace metals basis	790516-10G
Lithium bis(oxalato)borate	$LiB(C_2O_4)_2$	-	757136-25G
Lithium difluoro(oxalato)borate	$LiBF_2(C_2O_4)$	-	774138-25G
Lithium hexafluoroarsenate(V)	$LiAsF_6$	98%	308315-10G
Lithium hexafluorophosphate	$LiPF_6$	≥99.99% trace metals basis	450227-5G 450227-25G 450227-250G
Lithium perchlorate	$LiClO_4$	99.99% trace metals basis	634565-10G 634565-100G
Lithium phosphate monobasic	LiH_2PO_4	99%	442682-500G-A
Lithium tetrachloroaluminate	$LiAlCl_4$	99.99% trace metals basis	451142-5G
Lithium tetrachlorogallate	$LiGaCl_4$	99.99% trace metals basis	736317-5G
Lithium tetrafluoroborate	$LiBF_4$	99.99% trace metals basis	451622-5G 451622-25G
Lithium trifluoromethanesulfonate	CF_3SO_3Li	99.995% trace metals basis	481548-5G 481548-25G

Solvents and Additives

For a complete list of solvents and additives, visit aldrich.com/lib.

Product Name	Structure	Purity	Prod. No.
Acetonitrile, ACN	CH_3CN	99.999% trace metals basis	733466-1L 733466-4L
Allyl methyl sulfone, MAS		96%	718203-5G
Bis(trifluoromethane)sulfonimide lithium salt		-	449504-10G 449504-50G
1-Butyl-3-methylimidazolium methanesulfonate		99.9% trace metals basis	724394-5G
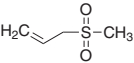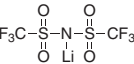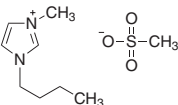
Solvents and Additives (Cont'd)

Product Name	Structure	Purity	Prod. No.
1-Butyl-3-methylimidazolium thiocyanate		≥95%	724408-5G
Diethyl carbonate		≥99%	517135-100ML 517135-1L
Diethyl sulfite, DES		98%	774278-25G
Dimethyl carbonate, DMC		≥99%	517127-100ML 517127-1L 517127-2L 517127-20L
1,2-Dimethyl-3-propylimidazolium bis(trifluoromethylsulfonyl)imide, DMPIIm		99.9% trace metals basis	724416-1G
Ethylene sulfite, ES		≥99.0%	774251-25G
Ethyl methyl carbonate, EMC		99%	754935-50ML
1-Ethyl-3-methylimidazolium tetrachloroaluminate		99.9% trace metals basis	724424-5G
Ethyl methyl sulfone		97%	709980-5G
Fluoroethylene carbonate, FEC		99%	757349-25G
3-(Methylsulfonyl)-1-propyne		95%	718319-5G
Methyl-trioctylammonium bis(trifluoromethylsulfonyl)imide		99.9% trace metals basis	724432-1G
Propylene carbonate		99.7%	310328-100ML 310328-500ML 310328-1L 310328-2L
1,2-Propyleneglycol sulfite, PS		≥98%	774456-10G
Propylene sulfate		≥99%	774294-10G
1,3-Propylene sulfite, TMS; PS		99.5%	774243-25G
Vinylene carbonate, VC		99%	757144-25G
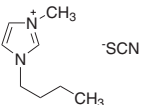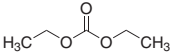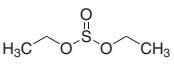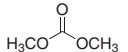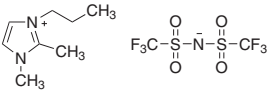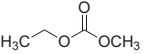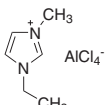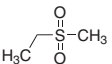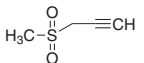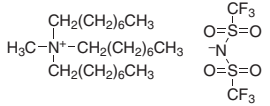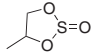
NANOWIRES
SMALL MATERIALS—BIG IMPACT

Aldrich® Materials Science enhances its nanowires offer with several new metallic, oxide, and ceramic nanomaterials with extremely high aspect ratios.

The basic properties of nanomaterials are directly related to their morphology, and one-dimensional nanostructures possess significant potential due to their combination of nanoscale diameters and macroscale lengths.

Nanowire materials have found applications in:

- Photovoltaics
- Piezoelectrics
- Electronics
- Nanocomposites
- Coatings
- Catalyst supports

Name	Composition	Dimensions (D × L)	Form	Prod. No.
Copper	Cu	100 nm × 20–30 μm	Suspension (isopropyl alcohol)	807931
Nickel(II) Oxide	NiO	~20 nm × ~10 μm	Nanowires	774545
Silver	Ag	20 nm × 12 μm	Suspension (isopropyl alcohol)	806714
Titanium(IV) Oxide	TiO_2	~10 nm × ~10 μm	Nanowires	774529
	TiO_2	~100 nm × ~10 μm	Nanowires	774510
Tungsten(VI) Oxide	WO_3	~50 nm × ~10 μm	Nanowires	774537
Zinc Oxide	ZnO	50 nm × 300 μm	Nanowires	773980
	ZnO	90 nm × 1 μm	Nanowires	773999
	ZnO	300 nm × 4–5 μm	Nanowires	774006

Tungsten(VI) Oxide Nanowires
Aldrich Prod. No. 774537
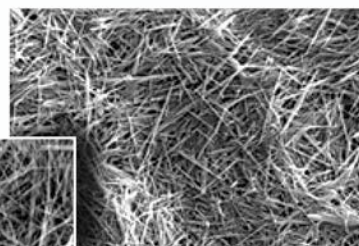
Titanium(IV) Oxide Nanowires
Aldrich Prod. No. 774510
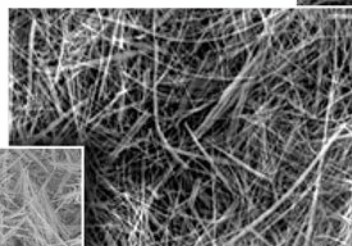
Zinc Oxide Nanowires
Aldrich Prod. No. 774006
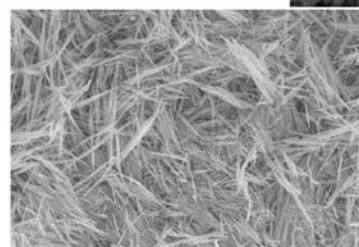
For the complete nanomaterials offering, visit
aldrich.com/nanowires

SIGMA-ALDRICH®

ELEMENTAL
BUILDING BLOCKS
FOR INNOVATIVE TECHNOLOGY

Goodfellow Alloys and Pure Elements Now Available

High-purity metals and alloys play an essential role in applications such as biomedical engineering and physical vapor deposition. Advances in materials science require materials that ensure optimum properties, performance, and quality. Over **9,900** elemental materials and **7,800** alloys are now available from Goodfellow Cambridge Ltd., a leading international supplier of metals and materials for research and industry.

As materials innovation requires not only the correct composition but also form, our selection of materials includes:

- Foils
- Rods
- Wires
- Tubes
- Fibers
- Bars
- Sheets
- Foams
- Honeycombs
- Spheres
- Powders
- Meshes

Goodfellow

Representative Materials

Name	Dimensions	Specifications	Prod. No.
Aluminum-Lithium-Copper Alloy	OD 24 mm; ID 22 mm	99% purity	GF55446295
Carbon, Fiber	0.007 mm diameter	Tex number 200, 3,000 filaments	GF20790558
Iron-Nickel Alloy	45 micron powder	99.9% purity	GF59815435
Tantalum, Tube	OD 0.31 mm; ID 0.19 mm	Trace metal purity, 99.9%	GF33615716
Niobium, Insulated Wire	0.125 mm diameter	Insulated wire, polyimide insulation	GF76912308

For a full selection of ultra-high purity materials, visit
go.sigmaaldrich.com/itselemental